X-621-76-41

PREPRINT

NASA TM X- 71105

TRAJECTORY TRACES OF CHARGED PARTICLES IN THE MAGNETOSPHERE

MASAKI EJIRI

MARCH 1976

GSFC

GODDARD SPACE FLIGHT CENTER

GREENBELT, MARYLAND

X-621-76-41

TRAJECTORY TRACES OF CHARGED PARTICLES IN THE MAGNETOSPHERE

Masaki Ejiri*
Laboratory for Planetary Atmospheres

*On leave from the Institute of Space and Aeronautical Science, University of Tokyo.

NASA/GODDARD SPACE FLIGHT CENTER
Greenbelt, Maryland 20771

TRAJECTORY TRACES OF CHARGED PARTICLES IN THE MAGNETOSPHERE

Masaki Ejiri
Laboratory for Planetary Atmospheres

ABSTRACT

The characteristic enhancements of ring current particles with energies of about 1 to 100 keV, associated with magnetospheric substorms, were observed by Explorer 45 (S^3-A) around the plasmapause in the afternoon to midnight region, and showed the characteristic structure called a 'nose' in the proton spectrograms. This paper describes the motion of these particles in the equatorial magnetosphere, under a recently proposed convection electric field and a dipole magnetic field. Approximate equations of a bounce period, a second adiabatic invariant and a bounce-average azimuthal velocity are given with inaccuracies less than about 10^{-3} for all pitch angles. The complete set of flow patterns of 90° pitch angle particles is also presented by means of stagnation lines through which radial drifts and/or azimuthal drifts change their directions. The particle tracings in the magnotosphere give a basic concept to explain the observed nose characteristics.

CONTENTS

TRAJECTORY TRACES OF CHARGED PARTICLES IN THE MAGNETOSPHERE

I. INTRODUCTION

There have been a number of observations of charged particles in the magnetosphere related to magnetospheric substorms [e.g., Vasyliunas, 1968; Shield and Frank, 1970; Lezniak and Winckler, 1970; DeForest and McIlwain, 1971; Frank, 1971]. It has been recognized that the convection electric field plays an important role in the motion of those particles [e.g., Taylor and Hones, 1965; Nishida, 1966; Kavanagh et al., 1968; McIlwain, 1972; Gurnett and Frank, 1973; Heikkila, 1974; Smith and Hoffman, 1974]. McIlwain (1973) deduced his electric field model with a specified injection boundary [Mauk and McIlwain, 1974] to explain ATS-5 particle data associated with substorms. Konradi et al (1975) followed McIlwain's model and showed that the substorm associated particles observed by Explorer 45 came from along or beyond the injection boundary. He also calculated the 27° pitch angle proton dispersion pattern and compared it with the 81° pitch angle protons.

Many theories have been developed about the charged particle motions in the magnetosphere under the convection electric field. Chen (1970) gave a morphology of 90° particle flow patterns assuming a uniform dawn-dusk electric field (see also references in his paper for other works). Stern (1975) calculated the particle energy change and showed some particle trajectories under the recently proposed convection electric field [Volland, 1973; Stern, 1974]. As for the off-90° pitch angle particle motions at the equator, several approximation methods to compute particle bounce period, second invariant and bounce average drift velocity have been investigated [Lew, 1961, Hamlin et al., 1961; Lencheck et al., 1961; Schultz, 1971; Chen and Stern, 1975]. But the off-90° particle trajectories in the magnetospheric equatorial plane have not been intensively studied yet.

Smith and Hoffman (1974) observed with Explorer 45 (S^3-A) the storm-time ring current proton enhancements and found in the 90° pitch angle proton spectrograms the characteristic 'nose' structures inside the plasmapause. They concluded that those particles came to the lower L-value region from the plasma sheet or tail regions under convection, corotation, and magnetic gradient and curvature drifts. An example of such data appears in Figure 1 in the form of spectrograms at eight different pitch angles for both outbound and inbound passes during the magnetic storm of February 13, 1972. (For a description of Explorer 45 and the particle detectors, see Williams et al., 1968, and Longanecker and Hoffman, 1973). Since the orbital plane was almost equatorial, pitch angles averaged over about 10 degrees. From the DC electric field experiment [Maynard and Cauffman, 1973;

Cauffman and Maynard, 1974], the plasmapause positions during the outbound and the inbound passes were identified as L = 5.1 and L = 4.8, respectively. It is obvious from these data that the typical 'nose' structure in each pitch angle spectrogram was observed inside the plasmapause. And, these structures definitely depend on particle energy and their pitch angles and the time-phase in the substorm. The higher pitch angle particles were detected at the lower L-value positions along both outbound and inbound orbits. The energy of the 'nose' edge was about 25 keV in the outbound and about 13 keV in the inbound for all pitch angles. Before the enhancements of energetic particles were observed, there were several substorm onsets identified from both high-latitude and low-latitude ground magnetograms.

To interprete these particle enhancements, especially the 1 keV-50 keV proton populations associated with substorms, we speculate the particle sources in the tail region which start to move towards the earth due to an enhancement or modification in the convection electric field. The simultaneous differential equations are deduced to present the motion of these particles in the equatorial plane, and approximate formulas for bounce period, second adiabatic invariant and bounce-average azimuth drift velocity of arbitrary pitch angle particle are given with sufficient accuracies of about 10^{-3}. Also, the 90° pitch angle flow patterns are delineated by means of stagnation lines (the definition of a stagnation line is given in V) through which particle flow directions are changed, giving complete morphology of particle motions in the equatorial plane by using the recently proposed convection electric field model of Volland and Stern [Volland, 1973; Stern, 1974, and 1975; Maynard and Chen, 1975]. The examples of particle tracings including off-90° pitch angle particles in the magnetosphere give a basic concept to explain the newly injected particle populations in the magnetosphere.

MKS units are adopted through this paper unless otherwise mentioned, and the symbols for quantities relevant to charged particle motion are listed in Appendix A.

II. A PREMISE

The equation of charged particle motion in a magnetic field $\vec{B}$ and an electric field $\vec{E}$ is given by

$$\frac{d}{dt}\left(m\frac{\vec{dr}}{dt}\right) = q\left(\frac{\vec{dr}}{dt} \times \vec{B} + \vec{E}\right) + \vec{F'}$$

where $\vec{r}$ is the position of the particle, q the particle charge, m the relativistic mass, and $\vec{F}'$ non-electromagnetic forces such as gravitational force, inertial force, gradient of pressure etc. Here we develop the above equation in a region where external forces $\vec{F}'$ may be neglected and a particle motion associated with a substorm injection may be well described by the non-relativistic equation ($m = m_0$, the rest mass of the particle). Furthermore, we assume the following conditions;

1. the geomagnetic field is a dipole field, its axis being perpendicular to the equatorial plane, and a field line is an equipotential,
2. changes in $\vec{E}$ and $\vec{B}$ are very slow, and the particle motion can be represented as a motion of its guiding center (cyclotron average drift motion, e.g., Northrop, 1963),
3. the particle motion is adiabatic, i.e., first and second adiabatic invariants (μ and J) are conserved,
4. there are no local energization and loss processes.

From the above basic equation, a guiding center drift velocity $\vec{u}_D$ in the equatorial plane is obtained, by averaging over a cyclotron motion and a bouncing motion between particle mirror points.

$$\vec{u}_D = \vec{F}_\perp \times \vec{B}/qB^2, \tag{1}$$

and

$$\vec{F}_\perp = q \cdot \vec{E} - q(\vec{\omega} \times \vec{R}) \times \vec{B} - W \cdot G(\alpha_0) \cdot \nabla_\perp B/B, \tag{2}$$

where $\vec{R}$ is the position vector from the center of the earth in the equatorial plane, W the particle kinetic energy, $\vec{\omega}$ the angular velocity of the earth, α_0 the particle pitch angle at the equator, and the function $G(\alpha_0)$ is given later.

The first term is a force due to an external electric field, the second term represents the corotation of the particle with a magnetic field line, and the third term shows the combined magnetic gradient and curvature drift. In the case $\alpha \neq 0°$, the particle kinetic energy W is written as

$$W = \mu B/y^2 \tag{3}$$

where $y = \sin\alpha_0$, and $\mu = W_\perp/B = 1/2\, mv_\perp^2/B$, the first adiabatic invariant. If $\alpha_0 = 90°$, the third term becomes a simple form,

$$-\mu\nabla_\perp B \tag{4}$$

Note that the conservation of the first invariant is of no avail if $\alpha_0 = 0°$ ($y = 0$). It is clear from equation (1) that the fundamental particle velocity vector direction in the midnight region is (i) earth-ward under a dawn-dusk convection electric field, (ii) eastward under the corotation field, and (iii) westward for protons and eastward for electrons under gradient-curvature drift. Combinations of these three kinds of drift motions make complicated particle flow lines which definitely depend on particle energy and pitch angle.

III. MOTION OF PARTICLES WITH ARBITRARY PITCH ANGLE

To solve equation (1) with initial conditions (R_i, y_i, W_i; $t = 0$) in given electric and magnetic fields, $\vec{E} = \vec{E}(R, P)$ and $\vec{B} = \vec{B}(R, P)$, where P is magnetic local time, we have to obtain the kinetic energy W or pitch angle y ($= \sin\alpha_0$) as a function of a particle position $\vec{R}(R, P)$, and a functional form of G(y) which is closely related to a particle bouncing motion in a mirror field.

There are three fundamental equations in connection with particle motion in a dipole field [e.g., Hamlin et al., 1961; Roederer, 1970], as follows:

1. Bounce period τ_b;

$$\tau_b = \frac{2}{v}\int_{s'_m}^{s_m} \frac{ds}{[1 - B(s)/B_m]^{1/2}} \equiv \frac{4R}{v} \cdot f(\alpha_0), \tag{5}$$

where

$$f(\alpha_0) = \int_0^{\lambda_m} \frac{\cos\lambda(1 + 3\sin^2\lambda)^{1/2}}{\{1 - \sin^2\alpha_0 \cdot \sec^6\lambda(1 + 3\sin^2\lambda)^{1/2}\}^{1/2}}\, d\lambda, \tag{6}$$

and

$$\sin^2\alpha_0 = \frac{\cos^6\lambda_m}{(1 + 3\sin^2\lambda_m)^{1/2}} \tag{7}$$

2. Second adiabatic invariant in the case of no parallel external force;

$$J = \oint p_{||}\, ds = 2pRI(\alpha_0) \tag{8}$$

where

$$I(\alpha_0) = 2\int_0^{\lambda_m} \left\{1 - \sin^2\alpha_0 \cdot \sec^6\lambda(1 + 3\sin^2\lambda)^{1/2}\right\}^{1/2} (1 + 3\sin^2\lambda)^{1/2} \cos\lambda d\lambda. \quad (9)$$

3. Bounce-average azimuthal drift velocity;

$$\frac{d\phi}{dt} = \frac{3mv^2}{2qk_0'} \cdot R \cdot \frac{g(\alpha_0)}{f(\alpha_0)}, \quad (10)$$

where

$$g(\alpha_0) = \int_0^{\lambda_m} \frac{\left\{2 - \sin^2\alpha_0 \cdot \sec^6\lambda(1 + 3\sin^2\lambda)^{1/2}\right\} (1 + \sin^2\lambda)\cos^3\lambda}{(1 + 3\sin^2\lambda)^{3/2}\left\{1 - \sin^2\alpha_0 \cdot \sec^6\lambda(1 + 3\sin^2\lambda)^{1/2}\right\}^{1/2}} d\lambda, \quad (11)$$

and

$$k_0' = a^3 k_0 = B/R^3.$$

After manipulation of equation (10), the third term of equation (2) can be obtained and $G(\alpha_0) = g(\alpha_0)/f(\alpha_0)$.

To understand the particle motion we must first compute an equatorial pitch angle change and a particle energy change due to radial drift motion. From equations (6) and (9), there is a relation of $f(\alpha_0)$ and $I(\alpha_0)$ in a differential form as

$$\frac{d}{dy}\left(\frac{I}{y}\right) = -\frac{2f}{y^2}, \quad (12)$$

where

$$y = \sin\alpha_0.$$

On the other hand, the constant of μ/J^2 gives

$$y = \frac{I(y)}{I(y_i)} \cdot \frac{L_i^{1/2}}{L^{1/2}} y_i. \quad (13)$$

Suffix (i) denotes initial values.

And, the conservation of μ gives (when $\mu \neq 0$)

$$\frac{d}{dL} (Wy^2 L^3) = 0. \tag{14}$$

The other form of energy change is given by Northrop and Teller (1960), and Kivelson and Southwood (1975),

$$dW/dR = qRB(d\phi/dt).$$

This equation can be transformed to a simple form as

$$\frac{dW}{dL} = -3G(\alpha_0) \frac{W}{L} . \tag{15}$$

Equations (14) or (15) give the energization rate of particle due to radial drift, which increases with a pitch angle increase.

Pitch Angle Change

For the equatorial pitch angle, Southwood and Kivelson (1975) suggested the approximate expression of

$$y \simeq \frac{y_i}{y_i + (1 - y_i)(L/L_i)^{0.45}} .$$

This is used as an initial condition for solving equation (13) by the Wegstein iteration method, after slight modification so that the right hand side of equation (13) never exceeds 1, i.e. $y = \sin\alpha_0 \leqslant 1$. This method has its advantage that the desired accuracy can be easily specified, if the value of I(y) is obtained with the same accuracy as discussed later. Figures 2a and 2b show changes in equatorial pitch angles, initial pitch angle being set at L = 10. The particles change their pitch angles less than 4 degrees in the region of L = 5 to 3. The calculation of particle trajectory, therefore, is done by tracing the same particle in spite of its pitch angle change as is shown in the figures, since the experimental data in the case of Explorer 45, for example, are averaged over the pitch angle interval of about 10 degrees (see Fig. 1). To compute a particle velocity vector, however, the change in pitch angle must be taken into account. Note that an equatorial pitch angle α_0 must satisfy the condition $\sin\alpha_0 > \sin\alpha_\ell = 1/\{L^3(4 - 3/L)^{1/2}\}^{1/2}$, where α_ℓ is an equatorial loss cone if we assume the mirror points above the earth's surface. This loss cone limit is also shown in the figures.

Particle Energy Change

The particle energization due to radial drift motion is calculated using equation (14) combined with equation (13) and the result is illustrated in Figure 3. The limiting cases for $\alpha_0 = 90°$ and $\alpha_0 = 0°$ are given simply as energy changes of $W_\perp$ and $W_{//}$ from first and second adiabatic invariants, respectively:

$$\begin{cases} W_\perp/W_{\perp i} = (L_i/L)^3 \text{ for } \alpha_0 = 90°, \\ W_{//}/W_{//i} = (L_i/L)^2 \text{ for } \alpha_0 = 0°. \end{cases} \tag{16}$$

The energy gain due to radial drift of the particle started from $L = 10$ is about 10 times in the region around $L = 4$, and the difference in energy between 0° and 90° pitch angle particles is 2.5 times. As is obvious from the form of equation (15), the energization rate is independent of initial energy. It is worthwhile to notice that, as for the gradient-curvature drift velocities of same energy particles with different pitch angles, the velocity of lower pitch angle particles is higher than the velocity of higher pitch angle particles in the region of high L-value. For example, in the case $W(90°) = W(0°)$ at $L = L'$, $W(0°)/W(90°) = (L_i/L')$ at $L = L_i$ and then the third term of equation (1) or equation (10) gives $d\phi/dt|_{0°}/d\phi/dt|_{90°} = (2/3)\,(L_i/L)$, since $G(0°) = 2/3$ and $G(90°) = 1$ (see Fig. 4). Therefore, $|d\phi(\alpha_0 = 0°)/dt| \geqslant |d\phi(\alpha_0 = 90°)/dt|$ in the region where $L_i \geqslant (3/2)L'$, in spite of $\mu(\alpha_0 \to 0°) \ll \mu(\alpha_0 = 90°)$.

Chen and Stern (1975) gave an approximate formula of energy as a function of $I(y)/y$. Cowley and Ashour-Abdalla (1975), Nakada et al., (1965), and others also show the changes in equatorial pitch angle and particle energy. To interprete the substorm associated particle enhancements in the ring current region, more important than the changes in pitch angle are the particle trajectories with time-development coupled with the changes in particle energy.

Approximations for f(y), I(y), and G(y)

In the calculations of particle trajectories by solving simultaneously the three differential equations as shown later, it is not practical to compute by integration the function values of f(y), I(y), and g(y) given by equation (6), (9), and (11), at every time step.

There have been many approximation formulas obtained by Lew (1961), Hamlin et al., (1961), Lencheck et al., (1961), Schulz (1971), and Chen and Stern (1975). Here a more accurate analytical approximation formula for f(y) is given, and I(y) and g(y) are deduced selfconsistently from f(y). Adopting Lencheck's approximation formula of f(y) as a zero order equation and adding higher order

terms of the form $y^{n/m}$ (n and m are integers), the best fit analytical expression is obtained in the case m = 3 and n = 1, 2, 3, and 4 in order to get the inaccuracy less than about 0.1% for all pitch angles, i.e.,

$$f(y) = \alpha - \beta(y + y^{1/2}) + a_1 y^{1/3} + a_2 y^{2/3} + a_3 y + a_4 y^{4/3} \tag{17}$$

where

$$\begin{aligned} a_1 + a_2 + a_3 + a_4 &= 0, \\ \alpha &= 1 + \ell n(2+\sqrt{3})/2\sqrt{3} \simeq 1.38, \end{aligned} \tag{18}$$

and

$$\beta = (\alpha/2) - (\pi/12)\sqrt{2} \simeq 0.32.$$

This equation gives exact values at y = 0 (0° pitch angle) and y = 1 (90° pitch angle). To determine the values of the coefficients a_1, .., and a_4 by the best fit of the approximation function given by equation (17) to the function f(y) of equation (16), we must compute an accurate functional value of f(y), the integrand of which has a singularity, by developing a special numerical integration method (see Appendix B). The results are;

$$a_1 = 0.055, a_2 = -0.037, a_3 = -0.074 \text{ and } a_4 = 0.056. \tag{19}$$

A similar approach has been used by Hilton (1971) to obtain McIlwain's function of L(I, B_m) and by Chen and Stern (1975) for W, f, and g as a function of I(y)/y.

Using analytical expression of f(y) in equation (17), I(y) is easily calculated from equation (12) (Schulz, 1971):

$$\begin{aligned} I(y) &= 2y \int_y^1 u^{-2} f(u) du \\ &= 2\alpha(1-y) + 2\beta y \ell n y + 4\beta(y - y^{1/2}) \\ &\quad + 3a_1(y^{1/3} - y) + 6a_2(y^{2/3} - y) + 6a_4(y - y^{4/3}) - 2a_3 y \ell n y. \end{aligned} \tag{20}$$

From equations (12) and (13), we have the differential form of the pitch angle change with respect to time t,

$$\frac{dy}{dt} = -\frac{y}{L} \cdot \frac{I(y)}{4f(y)} \cdot \frac{dL}{dt}. \tag{21}$$

Putting equations (21) and (15) into (14), the simple relation G(y), f(y), and I(y) is deduced as

$$G(y) \equiv \frac{g(y)}{f(y)} = 1 - \frac{I(y)}{6f(y)} . \tag{22}$$

Using equations (17) and (20), g(y) can be written as

$$\begin{aligned} 3g(y) = {} & 2\alpha - (5\beta - \alpha)y - (\beta - a_3)y\ell ny - \beta y^{1/2} \\ & + \frac{3}{2} a_1 y^{1/3}(1 - y^{1/3}) + 6a_4 y(y^{1/3} - 1). \end{aligned} \tag{23}$$

The computed functional forms of f(y), I(y), and G(y) are illustrated in Figures 3(a-c) as functions of equatorial pitch angle and colatitude of mirror point. To discuss qualitatively the trajectory of particles with arbitrary pitch angle in the equatorial plane, these figures together with Figures 2 and 3 are very useful (see equation (1)), though an actual particle trajectory can be obtained with a sufficient accuracy using the approximate expressions of f(y), I(y), and G(y) in equations (17), (20), and (22). The accuracies of approximations of these functions depend on the equatorial pitch angle, and are shown in Figure 5; the relative accuracy is calculated as 1 - (approximate value)/(true value). All these approximate functions have inaccuracies of about 10^{-3}. In the same figures are shown the results of Schulz's approximation (1971) evaluated again using accurate values of f(y) and I(y). The great improvements of the new approximations are evident from the figures. The expressions derived by Chen and Stern (1975) have accuracies of about 1.7%, but their variable $X = I(y)/y$ has a good advantage that $X \cdot L^{-1/2}$ is constant, whereas our variable y should be calculated using equation (13) or equation (21).

IV. ELECTRIC FIELD MODEL AND PARTICLE TRAJECTORIES

Charged particle flow patterns in the magnetosphere were first analyzed intensively by Chen (1970), assuming a constant dawn-dusk electric field and a dipole magnetic field. Subsequently, the observed plasmapause and plasma trough locations by Ogo 4, Ogo 5, and Ariel 3 have been interpreted, introducing a time dependency of the electric field strength as a function of Kp (interplanetary magnetic activity index) [Chen and Grebowsky, 1974; Grebowsky et al., 1974; Chen et al., 1975]. McIlwain, on the other hand, proposed his own electric field model E3 (1972) and E3H (1973) including a corotation field due to a rotation of a dipole magnetic field. The observed particle data of ATS-5 associated with substorms can be explained in his electric field model and the distorted magnetic field model M2.

Recently, based on the observed electric field data (Heppner, 1972) and the shape of the plasmapause, Volland (1973) and Stern (1974, 1975) proposed the following large scale potential fields as

$$\Phi_E = AR^{\gamma} \sin \phi. \tag{24}$$

Then,

$$\vec{E} = -\nabla \Phi_E \tag{25}$$

where A is a coefficient which determines the electric field intensity. Both of them reached the same exponent of $\gamma = 2$. Maynard and Chen (1975) succeeded to interpret the locations of the plasmapause and isolated cold plasma regions observed by Explorer 45, by using this model with $\gamma = 2$, A being a function of Kp as

$$A = \frac{0.045}{(1 - 0.159\,kp + 0.0093\,kp^2)^3} \quad (kV/R_E^2) \tag{26}$$

where R_E is an earth's radius. They deduced this Kp dependence from the plasmapause observations by Ogo 3 and 5, and this produces cross polar cap potentials similar to those found by Heppner (1973).

Using the corotation field expressed in equation (1), it can be readily obtained that the relation of a coefficient A in equation (24) with a stagnation point $R = R_0$ (or $L = L_0$) at dusk for zero energy particles is

$$A = -\frac{\kappa}{\gamma R_0^{\gamma}}, \tag{27}$$

and

$$\kappa = -a^3 k_0 \omega / R_0. \tag{28}$$

Hereafter, this electric field model represented in equations (25) to (28) is adopted.

Introducing a dimensionless distance x (distance normalized by R_0, i.e. $x = R/R_0 = L/L_0$ and $\vec{u}_D = R_0 \dot{\vec{x}}$), equation (1) can be written in polar coordinates (R, ϕ),

$$\frac{d}{dt}\vec{x} = \frac{dx}{dt}\hat{e}_R + x\frac{d\phi}{dt}\hat{e}_{\phi}, \tag{29}$$

where

$$\frac{dx}{dt} = -\omega \frac{x^{\gamma+2}}{\gamma}\cos\phi, \tag{30}$$

and

$$\frac{1}{\omega}\frac{d\phi}{dt} = x^{\gamma+1}\sin\phi + 1 - 3W \cdot G(y) \frac{1}{q\omega R_0^2 B} \cdot \frac{1}{x^2}. \tag{31}$$

The origin is the earth's center, and $\hat{e}_R$ and $\hat{e}_\phi$ are unit vectors. Equations (30) and (31) together with equation (21) are fundamental simultaneous differential equations of charged particle motion (the other forms of these equations are presented in Appendix C with conventional units). These equations do not contain explicitly the coefficient A of electric field strength which is only introduced in terms of scale factor R_0. From equations (27) and (28),

$$R_0 = \left(\frac{a^3 k_0 \omega}{\gamma A}\right)^{\frac{1}{\gamma+1}}. \tag{32}$$

In the case $\gamma = 2$,

$$L_0 = \frac{R_0}{a} \simeq 3.6/(A[kV/R_E^2])^{1/3}. \tag{33}$$

The Kp dependencies of the stagnation point at the dusk and midnight crossing points of the last closed equipotential line of zero energy particles are shown in Figure 6, using equations (26), (32), and (54) in the case of $\gamma=2$. In the steady electric field model these are identical to the plasmapause locations. McIlwain proposed a particle injection boundary from which energetic charged particles are injected into the magnetosphere at substorm onset time [McIlwain, 1973; Mauk and McIlwain, 1974; Konradi et al., 1975]. The radial distance of this injection boundary R_b is given as $R_b = (122-10\ Kp)/(\phi - 7.3)$ where R_b is in L-value and ϕ the local time in hours, and is illustrated also in Figure 6. This figure implies that McIlwain's injection boundary is far beyond the last closed equipotential line with an electric field strength used to explain the Explorer 45 plasmapause observations by Maynard and Chen (1975). The shapes of the injection boundary and the last closed equipotential line in the dusk to midnight region is discussed later (see also Fig. 8).

V. MOTION OF 90° PITCH ANGLE PARTICLES

From equations (30) and (31), fundamental equations of motion of 90° pitch angle particle (y = 1) are

$$\frac{dx}{dt} = -\omega \frac{x^{\gamma+2}}{\gamma} \cos\phi, \tag{34}$$

$$\frac{1}{\omega}\frac{d\phi}{dt} = x^{\gamma+1}\sin\phi + 1 - \frac{3\mu'}{x^2} \tag{35}$$

where

$$x = R/R_0 = L/L_0 \text{ and } \mu' = \mu/q\omega R_0^2. \tag{36}$$

To find the particle flow lines the time is eliminated from equations (34) and (35), and by integrating with respect to x and ϕ, we have

$$\frac{x^\gamma}{\gamma}\sin\phi - \frac{1}{x} + \frac{\mu'}{x^3} = c \tag{37}$$

where c is an integral constant.

This equation, as a matter of course, is identical to the conservation law of total energy of particle; $q\Phi + \mu B = C$ and $C(=\kappa qc)$ is an initial total energy conserved as a constant. The total potential Φ including convection field and corotation field is deduced from equations (24) and (1) as;

$$\Phi = \kappa\left(\frac{1}{x} - \frac{x^\gamma}{\gamma}\sin\phi\right) \tag{38}$$

where κ is from equation (28). The potential due to the corotation field is deducec from $\Phi_c = \int_\infty^R r\omega B(r)\,dr$, because a dipole magnetic field strength at the equator is expressed by a radial distance only. In a general distorted magnetic field, the corotation field cannot be represented by the gradient of a scalar field.

The families of equation (37) with various initial conditions c give the particle flow patterns, i.e., particles move along constant total energy lines. Stern (1975) studied the characteristic behavior of change in particle energy along the dawn-dusk line ($\phi = \pi/2$ and $3\pi/2$) using energy conservation law with $\gamma = 2$, and gave schematically two kinds of particle flow patterns. His definition of a

stagnation point is Δ(total energy) = 0 which is equivalent to both $dx/dt = 0$ and $d\phi/dt = 0$. Chen's calculation (1970) corresponds to the case $\gamma = 1$ and he also used the energy conservation law.

It is evident from equation (34) that $dx/dt = 0$ is only satisfied along the dawn-dusk line. But, in general the solution for $d\phi/dt = 0$ exists at an arbitrary local time ϕ, and henceforth we call this solution a "stagnation line", since through this line a particle flow direction changes from westward to eastward or vise versa, and particle velocities show their local minima along this line. The dawn-dusk line is also a stagnation line with respect to x, i.e., a particle flow direction is earthward in the nightside region and is outward in the dayside region. Figure 7 depicts one example of flow patterns (solid lines) of particles with $\mu' = 0.083$ in the orthogonal coordinate system, the ordinate being the normalized radial distance x and the abscissa the local time. The dashed lines represent the stagnation lines and the open arrows indicate the flow directions. The dashed areas are trapped regions or forbidden regions inside which any particles with the magnetic moment μ' never penetrate from the tail regions. As mentioned previously, this pattern is independent of electric field strength, only the scale factor R_0 being a function of electric field strength. In the figure the radius of the earth is 0.2 which corresponds to the stagnation distance $R_0 = 5a$.

Stagnation Lines and Last Closed Equipotential Line

Here we will discuss the stagnation lines for $d\phi/dt = 0$ in detail. Equation (31) is rewritten ($\rho = \sin\phi$) as;

$$f(x) \equiv \frac{1}{\omega}\frac{d\phi}{dt} = \rho x^{\gamma+1} + 1 - \frac{3\mu'}{x^2} = 0. \tag{39}$$

And,

$$\frac{d}{dt} f(x) = (\gamma+1)\rho^{-3}\left\{x^{\gamma+3} + \frac{6\mu'}{(\gamma+1)\rho}\right\}. \tag{40}$$

1. For $\rho\mu' > 0$;

   Since $f'(x)$ has a constant sign, $f(x)$ is a monotonically increasing ($\rho > 0$ and $\mu' > 0$) or decreasing ($\rho < 0$ and $\mu' < 0$) function, with one solution for $f(x) = 0$.

2. For $\rho\mu' < 0$;

$f'(x) = 0$ at x equal to

$$x_0 \equiv \left(\frac{-6\mu'}{(\gamma+1)\rho}\right)^{\frac{1}{\gamma+3}}, \tag{41}$$

and

$$f(x_0) = -\frac{\mu'}{|\mu|} \cdot 3\left(\frac{\gamma+3}{\gamma+1}\right)\left(\frac{\gamma+1}{6}\right)^{\frac{1}{\gamma+3}} \cdot |\rho^2\mu'^{(\gamma+1)}|^{\frac{1}{\gamma+3}} + 1. \tag{42}$$

2-1. For $\rho > 0$ and $\mu' < 0$, $f(x)$ is always positive and there is no solution for $f(x) = 0$.

2-2. For $\rho < 0$ and $\mu' > 0$, $f(x)$ and $f(x_0)$ are rewritten as

$$f(x) = -|\rho|x^{\gamma+1} + 1 - 3\mu'/x^2, \tag{43}$$

and

$$f(x_0) = 1 - \left\{\rho^2\left(\frac{\mu'}{\mu'_0}\right)^{\gamma+1}\right\}^{\frac{1}{\gamma+3}}, \tag{44}$$

where

$$\mu'_0 = \left(3 \cdot \frac{\gamma+3}{\gamma+1}\right)^{-\frac{\gamma+3}{\gamma+1}} \left(\frac{\gamma+1}{6}\right)^{-\frac{2}{\gamma+1}} \tag{45}$$

When $0 < \mu' \leqslant \mu'_0$, there always exist two roots (in the case $\mu' = \mu'_0$ and $|\rho| = 1$, two roots become one double root, since $f(x_0) = 0$). When $\mu'_0 < \mu'$, there is no solution for $|\rho| > \rho_0$ and two roots (one double root in the case $|\rho| = \rho_0$) for $|\rho| \leqslant \rho_0$,

where

$$\rho_0 = \left(\frac{\mu'_0}{\mu'}\right)^{\frac{\gamma+1}{2}} \tag{46}$$

3. For $\rho = 0$;

$$\text{one root of } x = \sqrt{3\mu'} \text{ independent of } \gamma. \tag{47}$$

4. For $\mu' = 0$;

$$\text{one root of } x = |\rho|^{-\frac{1}{\gamma+1}} \text{ when } \rho < 0, \tag{48}$$

and no solution when $\rho \geqslant 0$.

Though the above classifications are complete set of stagnation lines for $d\phi/dt = 0$, there exists another characteristic magnetic moment μ'_{00}, that is, one equipotential line passes through two stagnation points; one at dusk and another at dawn where $d\phi/dt = dx/dt = 0$. This magnetic moment μ'_{00} is obtained by a numerical method from equations (37) and (39).

Examples of 90° pitch angle particle flow lines and their stagnation lines are calculated in the case $\gamma = 2$. Firstly, the last closed equipotential line for $\mu = 0$ is shown in Figure 8. This line plays an important role in the formation of the plasmapause if we assume the convection electric field to be time-independent, because this line is also a boundary of the zero energy particle forbidden region inside which particles are trapped and outside which particles take open trajectories. In general, the equation of this equipotential line is deduced from equation (37), c being determined at $x = 1$ and $\rho = -1$.

$$\rho x^{\gamma+1} + (\gamma + 1)x - \gamma = 0. \tag{49}$$

In the case $\gamma = 1$, this is a simple quadratic equation and studied by Chen and Wolf (1972). In the case $\gamma = 2$, x is represented in terms of ρ (= $\sin\phi$) as

(i) For $\rho = 0$ ($\phi = 0$ or π),

$$x = 2/3. \tag{50}$$

(ii) In the morning side where $0 < \rho$,

$$x = \left\{(\sqrt{1+\delta}+1)^{1/3} - (\sqrt{1+\delta}-1)^{1/3}\right\} \cdot \delta^{1/3}. \tag{51}$$

In the afternoon (dusk) side where $\rho < 0$,

$$x = 2 \cdot \sqrt{\delta} \cos\left(\frac{\theta+\pi}{3}\right), \tag{52}$$

and the other solution ($x \geqslant 1$) is

$$x = 2 \cdot \sqrt{\delta} \cos\left(\frac{\theta+5\pi}{3}\right), \tag{53}$$

where $\delta = 1/|\rho|$ and $\theta = \cos^{-1}\sqrt{|\rho|}$; $0 \leqslant \theta < \pi/2$.

In Figure 8 both cases ($\gamma = 1$ and $\gamma = 2$) are shown, together with McIlwain's injection boundary by the dashed line (see previous section). The dash-dotted lines are stagnation lines discussed above; $x = 1/\sqrt[3]{|\sin\phi|}$ for $\gamma = 2$ and similarly $x = 1/\sqrt{|\sin\phi|}$ for $\gamma = 1$ when $\rho < 0$. Note that the shape of McIlwain's injection boundary normalized by the stagnation point at dusk coincides well with the last closed equipotential line with $\gamma = 2$, while the unnormalized distance is far beyond that deduced from equations (26) and (32). (See Fig. 6). The ratio of crossing points at dusk, midnight and dawn meridians is

$$1 : 2/3 : (\sqrt{2}+1)^{1/3} - (\sqrt{2}-1)^{1/3} \simeq 1 : 0.67 : 0.60 \tag{54}$$

Particle Flow Patterns With $\gamma = 2$

In the case $\gamma = 2$, μ'_{00} and μ'_0 are calculated as

$$\begin{cases} \mu'_{00} \simeq 0.064 \\ \mu'_0 = 2^{2/3} \cdot 5^{-5/3} \simeq 0.109. \end{cases} \tag{55}$$

In order to identify what flow pattern an observed particle takes in the magnetosphere, it is convienient to utilize Figure 9, which illustrates the relation of the normalized magnetic moment μ' and μ with various stagnation distance L_0 given by equation (36). The upper part of the figure shows a particle energy corresponding to the magnetic moment indicated in the abscissa. For example in the case $L_0 = 5$, μ'_{00} and μ'_0 correspond to magnetic moment μ of about 0.0047 and 0.008 [keV/gamma] and their particle energies are about 2.3 and 3.9 keV at $L = 4$, respectively. The other example is as follows. If the plasmapause

position was observed at $R = R_p$ and $\phi = \phi_p$, then equation (51) or (52) gives the stagnation point L_0 at dusk. Using a line labeled L_0, the observed particle energy and position give directly the normalized magnetic moment μ' which indicates which flow pattern that observed particle took.

A complete set of particle flow patterns classified on the basis on the characteristic magnetic moments, i.e. $\mu' = 0$, μ'_{00} and μ'_0, is shown in Figures 10(a-g). Solid lines represent particle trajectories, flow directions being indicated by arrows. Dashed lines are stagnation lines, and A, B, and C are stagnation points. The hatched area is a forbidden region and, roughly speaking, positive particles go around eastward where the corotation drift exceeds the gradient-B drift and vice versa. The double-hatched area is also a forbidden or trapped region, but particles inside this region never make a complete circle around the earth. The size of the earth in the figures is $x = 0.2$, i.e. one fifth of the zero energy particle stagnation distance R_0 at dusk. This can be changed according to the scale factor R_0 or L_0 as $x_{earth} = a/R_0 = 1/L_0$.

1. Electrons, $\mu' < 0$, Figure 10a:

   The flow pattern of electrons is illustrated in Figure 10a for the case $\mu' = -0.2$. Since directions of gradient-B drift and corotation drift are the same sense, i.e. eastward, the radial distance of the stagnation point A at dusk is always greater than 1. This indicates that any electrons injected from the tail or plasma sheet region never penetrate inside the plasmapause under the steady state convection electric field. The radial distance of the last closed equipotential line that is a boundary of a forbidden region increases as μ' decreases.

2. Zero energy particle, $\mu' = 0$, Figure 10b:

   Figure 10b shows the particle flow pattern of zero energy particles. The last closed equipotential line (or flow line) has been discussed previously in detail (see Fig. 8). Previously it was a misleading thought that the boundary inside which the corotation field is dominant and outside which the convection electric field becomes more important is a last closed equipotential line or plasmapause location [e.g. Chen, 1970]. Strictly the boundary of electric field dominance is expressed in the simple form as $x = 1$ for $\gamma = 1$, and $x = \left\{2/\sqrt{1 + 3\rho^2}\right\}^{1/3}$ for $\gamma = 2$; the latter is represented by the chain circle in the figure, whereas the last closed equipotential line is a boundary of the forbidden region (hatched area in the figure) given by equations (51) and (52). With respect to the potential field the boundary of potential field dominance becomes $x = \sqrt{1/|\rho|}$ for $\gamma = 1$, and $x = \sqrt[3]{2/|\rho|}$ for $\gamma = 2$; the former is identical to

the stagnation line in the afternoon to midnight region. The stagnation line indicated by a dashed line is a boundary, in the earth-side region of which the eastward drift due to corotation field exceeds the westward drift due to convection field for $\pi \leqslant \phi \leqslant 2\pi$, i.e. in the afternoon to midnight. In the region, $0 < \phi < \pi$, both drifts are eastward. Suffice it to say that this stagnation line is very important for knowing the particle flow directions. Since $\mu' = 0$, corotation and convection electric fields are simply balanced at the stagnation point A at dusk. Thus this distance R_0 represents the strength of the convection electric field. When the convection electric field is not steady, that is, time-dependent, a last equipotential line is no longer a plasmapause position.

3. Particles with $\mu' > 0$.

The flow pattern of positive particle with non-zero magnetic moment becomes more complex due to the gradient-B drift, the flow direction of which is opposite to that of corotation drift.

(i) $0 < \mu' < \mu'_{00}$, Figure 10c:

The flow pattern of particles with $\mu' = 0.029$ is illustrated in Figure 10c. The size of the forbidden region becomes slightly smaller than that for zero energy particles. The stagnation line BC appears circled around the earth inside the forbidden region and its area increases as μ' increases, until the point C coincides with the point D. Inside the circle the westward drift mainly due to the gradient-B drift dominates the corotation drift, and the particle near that stagnation lines does not make a complete circle around the earth, just drifting around the stagnation point B.

(ii) $\mu' = \mu'_{00}$, Figure. 10d:

When μ' is equal to the characteristic magnetic moment $\mu'_{00} \simeq 0.064$, the stagnation line inside the forbidden region comes in contact with the last closed equipotential line at the point C = D, as shown in Figure 10d. The flow pattern is similar to the previous one (Fig. 10c), but there is no particle that makes a complete circle around the earth eastward. The inner equipotential line through the point C is an innermost open trajectory of the particle which is accessible from the tail region, because the forbidden region is separated into two parts by this line when μ' exceeds μ'_{00}. Note that particles on the equipotential lines through A and C take an infinite time to move around the earth.

(iii) $\mu'_{00} < \mu' < \mu'_0$, Figure 10e:

The flow pattern is shown in Figure 10e for the case $\mu' = 0.083$. The same particle flow pattern is illustrated in Figure 7 in a rectangular coordinate system to explain the relation of particle flow directions with stagnation lines. The separated trapped region appears at the dusk side, in which all particles move around the inner stagnation point B. In the forbidden region around the earth all particles drift westward due to gradient-B drift. Between the two separated forbidden regions there is a channel through which particles can penetrate closer to the earth along the open trajectory from the tail. The inmost distance of this trajectory is in the dusk meridian and increases as the magnetic moment increases.

(iv) $\mu' = \mu'_0$, Figure 10f:

When μ' is equal to the characteristic magnetic moment $\mu'_0 \simeq 0.109$, the stagnation point A coincides with the point B, i.e. two stagnation lines seen in the case $0 < \mu' < \mu'_0$ join with each other at this point, and the isolated trapped region vanishes away. Figure 10f delineates the particle flow pattern of this case. All particles inside the forbidden region drift around the earth westward because of the dominance of the gradient-B drift over the other two drifts. The point A (= B) is an inmost stagnation point at dusk; the distance is about $x \simeq 0.74$.

(v) $\mu'_0 < \mu'$, Figure 10g:

As the magnetic moment μ' increases and exceeds the characteristic magnetic moment μ'_0, there exists only one stagnation point at dawn, no stagnation point at dusk, and only one stagnation line, as illustrated in Figure 10g for the case $\mu' = 0.2$. The particle flow pattern for $\mu' > \mu'_0$ is apparently similar to those of a zero energy particle or electrons, if the directions of dawn and dusk are exchanged around the noon-midnight meridian. The stagnation line, however, is distinctly different for each case; that is, there always exists particles which change their flow directions four times in the case $\mu' > \mu'_0$, whereas there are no such electrons or zero energy particles. In other words, the stagnation line for $\mu' > \mu'_0$ in the afternoon to midnight region never vanishes, while there is no stagnation line for $\mu' \leqslant 0$ in the midnight to afternoon region.

VI. TIME-DEPENDENT PARTICLE FLOWS

The observational data of energetic particles associated with substorms show complicated but clear particle enhancements around or inside the plasmapause [Smith and Hoffman, 1974]. Trajectories of those particles which are presumably injected from the plasma sheet or tail region and drift in the magnetosphere are strongly dependent on particle energy and pitch angle due to a combination of convection, corotation, and gradient-curvature drifts.

To understand the fundamental particle motion in the magnetosphere, the 90° pitch angle particle motion is studied in detail, and a complete set of flow patterns is presented, taking into account the stagnation lines along which $d\phi/dt = 0$; the stagnation line for $dx/dt = 0$ is a dawn-dusk meridian line. Although those patterns explain the energy-dependent and complicated trajectories of particles, the drift time along the trajectory can not be deduced from the energy conservation law and is not indicated in the figures. To interpret the observed enhancements of injected particles, more important is a dynamical motion of the particles or a particle tracing with respect to the time-phase of a substorm and the observational time.

Using the three simultaneous differential equations in (C-1) to (C-4), particle trajectories in the magnetosphere are simulated. In Figures 11(a-h) are illustrated some examples of results for 90° pitch angle particles, which display the energy dependence on the particle trajectories. The initial particle source location is assumed to be at $L = 10$ and $20{:}00\ \text{MLT} \leqslant \phi < 4{:}00\ \text{MLT}$ at 0.1 hour intervals. The initial particle energies range from -0.4 keV to 51.2 keV for Figures 11(a-l). The strength of the convection electric field is represented by the stagnation distance $L_0 = 5$, which corresponds to $A = 0.057\ [\text{mV/m}\cdot R_E]$ and an electric field intensity of 0.57 [mV/m] at $L = 10$ in the midnight. From equation (26) this is the case for $Kp \simeq 4.1$. The particle positions are plotted at 0.1 hour steps by dots and at 1 hour steps by asterisks, within 20 hours and $L \leqslant 10$. These particle traces can be easily classified into the categories of particle flow patterns given in Figure 10, by means of the relation of μ' (normalized magnetic moment) and W (particle energy) or μ in Figure 9; (a) to Figure 10(a), (b) to Figure 10(b), (c) to Figure 10(c), (d) to Figure 10(e), and (e) $\sim$ (l) to Figure 10(g). In these particle trajectories, therefore, Figure 11(d) shows the inmost accessible trajectory to the earth if the infinite time of particle travelling is considered. But, as is evidently understood in these figures the inmost accessible distance strongly depends on particle travelling time from the source region as well as particle energy. This is the main cause of the formation of a 'nose' structure inside the plasmapause observed by S^3-A [Smith and Hoffman, 1974].

In the midnight region, particles with energies less than about 10 keV at L = 10 come from L = 10 to L = 9 in about 6 min, to L = 8 in about 18 min, and L = 7 in about 36 min, which are determined mainly by the convection drift velocity. A rough estimate of the convection speed 0.1 R_E/min beyond the synchronous orbit from ATS-1 magnetic field variations derived by Parks et al. (1971) are in the range of this result: 0.17 R_E/min to 0.06 R_E/min. Also, the electric field intensity at synchronous orbit used in this calculation is 0.376 mV/m which coincides well with the value of 0.36 mV/m by Shelley et al. Note that this convection electric field is a function of magnetic activity and position given in Equations (24) and (25).

Ambiguity in the source location of the particles does not affect much the particle trajectories given in the figures since the front of the particle trajectories, i.e. all particle locations at a fixed time beyond the synchronous orbit, is almost irrespective of particle energy, pitch angle and charge. Therefore, only the time marks need be shifted so that the time of the particles at a source location is a starting time. For example in the case of a particle source location at L = 8 at midnight, the first asterisk shows the location of a particle at the time of +0.7 hour, etc.

Although these trajectories are immutable with respect to the convection electric field strength as previously mentioned, the actual particle locations are very sensitive to the change in distance of the stagnation point, because of changes of both scale factor and trajectory due to change of magnetic moment (see equations (32) and (36)). For the higher energy particles shown in Figure 11(k-l), the trajectories look very different. There are no particles at the dawn meridian, and futhermore particles are unable to come inside the synchronous orbit, but are swept out towards the dayside magnetopause very rapidly.

Figures 12(a-d) illustrate the difference of particle trajectory due to pitch angles. The particle initial energy at L = 10 is 0.566 keV and their pitch angles are (a) 0°, (b) 30°, (c) 60°, and (d) 90°. As is shown in Figure 3 the energies of particles with different pitch angles change with L at different energization rates, and particles take quite different trajectories especially inside the synchronous orbit. This means that particles with the same energy but different pitch angles starting from the same source location are dispersed to different locations according to their energy and pitch angle. This may be the main cause of pitch angle anisotropies found in the vicinity of the proton 'nose' structures associated with substorms [Ejiri et al., 1975]. For most of substorm associated particles with energies of about 1 keV to 30 keV inside the plasmapause in the dusk side, particles with large pitch angles penetrate to lower L-values than particles with small pitch angles. This is clearly seen in Figure 13 which shows the locations of particle fronts for particles with 0° and 90° pitch angles; other pitch angle particle

fronts are located between these two lines. From this figure we can speculate a quite different pitch angle anisotropy in the morning side, i.e. inverse anisotropy to that in the evening side. The distance between different pitch angle particle fronts changes with travelling time and depends on the local time meridian to be considered as well.

The convection electric field used in this calculation is time-independent. Recently Roederer and Hones (1974) developed a time-dependent electric field model to interpret the ATS-5 particle data. Though the electric field as a function of Kp is time-dependent, the time resolution of 3 hours is not sufficient to interpret the particle enhancements during substorm expansion phase.

The detailed descriptions of observational data of Explorer 45(S^3 -A) and their interpretations using particle tracings developed in this paper will be presented in a separate paper.

VII. ACKNOWLEDGMENTS

I wish to express my sincere thanks to Drs. R. A. Hoffman and P. H. Smith for their encouragement and valuable discussions, especially for providing unpublished Explorer 45 particle data that motivated much of this work, and to Drs. D. P. Stern, A. J. Chen, M. Sugiura, and K. Maeda for their comments and suggestions. I am grateful to Christine Gloeckler, Christine J. McQuillan and Dr. Narindra K. Bewtra for assistance in the computer programming and displays. I am also indebted to NAS/NRC for sponsoring my Post-Doctor Research Associateship in the Laboratory for Planetary Atmospheres, NASA/GSFC.

VII. REFERENCES

Cauffman, D. P. and N. C. Maynard, "A Model of the Effect of the Satellite Photosheath on a Double Floating Probe System", J. Geophys. Res., 79, 2427-2438, 1974.

Chen, A. J., "Penetration of Low-energy Protons Deep into the Magnetosphere", J. Geophys. Res., 75, 2458-2467, 1970.

Chen, A. J., and R. A. Wolf, "Effects on the Plasmasphere of a Time-varying Convection Electric Field", Planet. Space Sci., 20, 483-509, 1972.

Chen, A. J., and J. M. Grebowsky, "Plasma Tail Interpretations of Pronounced Detached Plasma Regions Measured by OGO 5", J. Geophys. Res., 79, 3851-3855, 1974.

Chen A. J., and J. M. Grebowsky, and H. A. Taylor, Jr., "Dynamics of Mid-latitude Light Ion Through and Plasma Tails", J. Geophys. Res., 80, 968-976, 1975.

Chen, A. J., and D. P. Stern, "Adiabatic Hamiltonian of Charged Particle Motion in a Dipole Field", J. Geophys. Res., 80, 690-693, 1975.

Cowley, S. W. H., and M. Ashour-Abdalla, "Adiabatic Plasma Convection in a Dipole Field: Variation of Plasma Bulk Parameters with L", Planet. Space Sci., 23, 1527-1549, 1975.

DeForest, S. E., and C. E. McIlwain, "Plasma Clouds in the Magnetosphere", J. Geophys. Res., 76, 3587-3611, 1971.

Ejiri, M., R. A. Hoffman, and P. H. Smith, "Model Calculations of Particle Traces in the Magnetosphere - the Nose Structure of Ring Current Proton Enhancements Observed by Explorer 45 (S^3 -A)", Trans. Am. Geophys. Union, EOS, 56, No. 12, 1047, 1975.

Frank, L. A., "Plasma in the Earth's Polar Magnetosphere", J. Geophys. Res., 76, 5202-5219, 1971.

Grebowsky, J. M., Y. Tulunay, and A. J. Chen, "Temporal Variations in the Dawn and Dusk Midlatitude Through and Plasmapause Positions", Planet. Space Sci., 22, 1089-1099, 1974.

Gurnett, D. A., and L. A. Frank, "Observed Relationships Between Electric Fields and Auroral Particle Precipitation", J. Geophys. Res., 78, 145-170, 1973.

Heikkila, W. J., "Outline of Magnetospheric Theory", J. Geophys. Res., 79, 2496-2500, 1974.

Hamlin, D. A., R. Karplus, R. C. Vik, and K. M. Watson, "Mirror and Azimuthal Drift Frequencies for Geomagnetically Trapped Particles", J. Geophys. Res., 66, 1-4, 1961.

Heppner, J. P., "Electric Field Variations During Substorms: OGO 6 Measurements", Planet. Space Sci., 20, 1475-1498, 1972.

Heppner, J. P., "High-latitude Electric Fields and the Modulations Related to Interplanetary Magnetic Field Parameters", Radio Sci., 8, 933-948, 1973.

Hilton, H. H., "L Parameters, a New Approximation", J. Geophys. Res., 76, 6952-6954, 1971.

Kavanagh, L. D. Jr., J. W. Freeman, Jr., and A. J. Chen, "Plasma Flow in the Magnetosphere", J. Geophys. Res., 73, 5511-5519, 1968.

Kivelson, M. G., and D. J. Southwood, "Local Time Variations of Particle Flux Produced by an Electrostatic Field in the Magnetosphere", J. Geophys. Res., 80, 56-65, 1975.

Konradi, A., C. L. Semar, and T. A. Fritz, "Substorm-injected Protons and Electrons and the Injection Boundary Model", J. Geophys. Res., 80, 543-552, 1975.

Lenchek, A. M., S. F. Singer, and R. C. Wentworth, "Geomagnetically Trapped Electrons from Cosmic Ray Albedo Neutrons", J. Geophys. Res., 66, 4027-4046, 1961.

Lew, J. S., "Drift Rate in a Dipole Field", J. Geophys. Res., 66, 2681-2685, 1961.

Lezniak, T. W., and J. R. Winckler, "Experimental Study of Magnetospheric Motions and the Acceleration of Energetic Electrons during Substorms", J. Geophys. Res., 75, 7075-7098, 1970.

Longanecker, G. W., and R. A. Hoffman, "S^3 -A Spacecraft and Experimental Description", J. Geophys. Res., 78, 4711-4717, 1973.

Mauk, B. H., and C. E. McIlwain, "Correlation of Kp with the Substorm-injected Plasma Boundary", J. Geophys. Res., 79, 3193-3196, 1974.

Maynard, N. C., and D. P. Cauffman, "Double Floating Probe Measurements on S^3 -A", J. Geophys. Res., 78, 4745-4750, 1973.

Maynard, N. C., and A. J. Chen, "Isolated Cold Plasma Regions: Observations and Their Relation to Possible Production Mechanisms", J. Geophys. Res., 80, 1009-1013, 1975.

McIlwain, C. E., "Plasma Convection in the Vicinity of Geosynchronous Orbit", Earth's Magnetospheric Processes, ed. B. M. McCormac, 268-279, D. Reidel Pub. Co. Dordrecht-Holland, 1972.

McIlwain, C. E., "Substorm Injection Boundaries", paper presented at the Chapman Memorial Symposium, NOAA, Boulder, Colorado, June, 1973.

Nakada, M. P., J. W. Dungey, and W. N. Hess, "On the Origin of Outer-belt Protons, 1", J. Geophys. Res., 70, 3529-3532, 1965.

Nishida, A., "Formation of Plasmapause, or Magnetospheric Plasma Knee, by the Combined Action of Magnetospheric Convection and Plasma Escape from the Tail", J. Geophys. Res., 71, 5669-5679, 1966.

Northrop, T. G., and E. Teller, "Stability of Adiabatic Motion of Charged Particles in the Earth's Field", Phys. Rev. 117, 215-225, 1960.

Northrop, T. G., The Adiabatic Motion of Charged Particles, New York, Interscience Publishers, 1963.

Parks, G. K., E. H. Gardner, C. S. Lin, R. E. Newell, and P. J. Wehrenberg, "Interplanetary Control of Magnetosphere Dynamics", Correlated Interplanetary and Magnetospheric Observations, ed. D. E. Page, 49-60, D. Reidel Pub. Co. Dordrecht-Holland, 1974.

Roederer, J. G., Dynamics of Geomagnetically Trapped Radiation, Physics and Chemistry in Space 2, New York, Springer-Verlag, 1970.

Roederer, J. G., and E. W. Hones, Jr., "Motion of Magnetospheric Particle Clouds in a Time-dependent Electric Field Model", J. Geophys. Res., 79, 1432-1438, 1974.

Schield, M. A., and L. A. Frank, "Electron Observations Between the Inner Edge of the Plasma Sheet and the Plasmasphere", J. Geophys. Res. 75, 5401-5414, 1970.

Schulz, M., "Approximate Second Invariant for a Dipole Field", J. Geophys. Res., 76, 3144-3148, 1971.

Shelley, E. G., R. G. Johnson, and R. D. Sharp, "Plasma Sheet Convection Velocities Inferred from Electron Flux Measurements at Synchronous Altitude", Radio Sci., 6, No. 2, 305-313, 1971.

Smith, P. H., and R. A. Hoffman, "Ring Current Particle Distributions during the Magnetic Storms of December 16-18, 1971", J. Geophys. Res., 78, 4731-4737, 1973.

Smith, P. H., and R. A. Hoffman, "Direct Observations in the Dusk Hours of the Characteristics of the Storm Time Ring Current Particles During the Beginning of Magnetic Storms", J. Geophys. Res., 79, 966-971, 1974.

Southwood, D. J., and M. G. Kivelson, "An Approximate Analytic Description of Plasma Bulk Parameters and Pitch Angle Anisotropy Under Adiabatic Flow in a Dipolar Magnetospheric Field", J. Geophys. Res., 80, 2069-2073, 1975.

Stern, D. P., "Models of the Earth's Electric Field", NASA/GSFC, preprint, X-602-74-159, May, 1974.

Stern, D. P., "The Motion of a Proton in the Equatorial Magnetosphere", J. Geophys. Res., 80, 595-599, 1975.

Sugiura, M., and S. Chapman, "Tables and Figures Related to the Geomagnetic Dipole Field", NASA/GSFC, document X-612-66-546, December, 1966.

Taylor, H. E., and E. W. Hones, Jr., "Adiabatic Motion of Auroral Particles in a Model of the Electric and Magnetic Fields Surrounding the Earth", J. Geophys. Res., 70, 3605-3628, 1965.

Vasyliunas, V. M., "A Survey of Low-energy Electrons in the Evening Sectors of the Magnetosphere With OGO 1 and OGO 3", J. Geophys. Res., 73, 2839-2884, 1968.

Volland, H., "A semiempirical Model of Large-Scale Magnetospheric Electric Fields", J. Geophys. Res., 78, 171-180, 1973.

Williams, D. J., R. A. Hoffman, and G. W. Longanecker, "The Small Scientific Satellite (S^3) Program and its First Payload", NASA/GSFC, Preprint X-612-68-418, 1968.

APPENDIX A

The following symbols are used in the text:

a	earth's radius (6.371×10^6 m)
α_0	equatorial pitch angle
$\vec{B}$	dipole magnetic field; $B = k_0/L^3$ at equator
B_m	B at $\lambda = \lambda_m$
$\vec{E}$	electric field; $\vec{E} = -\nabla\Phi$[V/m]
J	second (longitudinal) adiabatic invariant
k_0	magnetic field strength at L = 1 (0.31×10^{-4} Wb/m^2)
L	McIlwain's L-value; R = aL
λ	latitude
λ_m	mirror latitude
μ	first adiabatic invariant (magnetic moment); $\mu = p^2/2m$
p	particle momentum; p = mv
Φ	electric potential
ϕ	local time in radian
q, m	particle charge (negative for electrons) and mass
$\vec{R}$	particle guiding center position at equator
R_0	stagnation distance at dusk for zero energy particle; $R_0 = aL_0$
s	length along the magnetic field line
s_m, s'_m	mirror points
t	time
v	particle velocity
W	particle kinetic energy
ω	angular velocity of the earth

($\perp$ and $\parallel$ denote the components perpendicular and parallel to the magnetic field line, respectively)

APPENDIX B

To obtain an accurate value of integration of equation (6), the integrand of which has a singularity, the integral $f(\alpha_0)$ is divided into two parts, i.e.

$$f(\alpha_0) = f_0(\alpha_0) + f_1(\alpha_0) = \int_0^{1-H} F(z)dz + \int_{1-H}^{1} F(z)dz \qquad \text{(B-1)}$$

where

$$z = \sin\lambda/\sin\lambda_m .$$

The integrand of the second term is expanded around the singular point as

$$F(z) = g_1(a)\left\{h^{-1/2} + g_2(a)h^{1/2} + 0(h)^{3/2}\right\} \qquad \text{(B-2)}$$

where

$$z = 1 - h;\ h\epsilon[1-H, 1],$$

$$a = \sin\lambda_m (a \neq 1),$$

$$g_1(a) = (1 + 3a^2)\sqrt{1-a^2}/\sqrt{3(3-5a^2)},$$

and

$$g_2(a) = (60a^6 + 19a^4 - 12a^2 + 3)/4(1 + 3a^2)(1 - a^2)(3 + 5a^2).$$

Then, the integration of F(z) in a region [1-H,1] becomes

$$f_1(\alpha_0) = \int_{1-H}^{1} F(z)dz = g_1(a)\left\{2H^{1/2} + 2/3g_2(a)H^{3/2} + 0(H^{5/2})\right\}. \qquad \text{(B-3)}$$

The integral $f_0(\alpha_0)$ can be computed with a specified accuracy by usual numerical integration methods, since the functional values of F(z) and its n-th derivative have finite values in the region [0, 1-H]. From equation (B-3), we have the value of $f(\alpha_0)$ with an accuracy of $H^{5/2}$; for instance if H is 10^{-6}, then $0(H^{5/2}) \sim 10^{-15}$. It is further recommended to divide the region [0, 1-H] into several regions and to use a sufficiently small step corresponding to each integral region,

keeping the same accuracy. In order to get the accuracy of 10^{-8} by the Hermitian fourth order integration method, the region is divided as $[1 - 10^{-n}, 1 - 10^{-(n+1)}]$; $n = 0, 1, \ldots 5$, and a numerical integral step of $\Delta h = 0.9/10^{n+3}$ is used. This method reduces the number of calculating steps to the amount 10^{-4}, compared with the case of a constant integral step used throughout the region.

The integral $I(\alpha_0)$ has no singularity in the integrand but its derivative has the same kind of singularity as $F(z)$. The above method therefore, should be used.

This method can be applicable to any integral in the case of its integrand or its n-th derivative having any singular points. Sigiura and Chapman (1966) developed another method of integration and gave the functional values of $f(\alpha_0)$ and $I(\alpha_0)$ with an accuracy of 10^{-7} at 1° intervals of mirror latitude.

APPENDIX C

For practical use, equations (30), (31), and (21) are transformed, with change of the units ($y \neq 0$) into

$$\frac{dx}{dt} = C_1 \frac{x^{\gamma+2}}{\gamma} \cos\phi', \tag{C-1}$$

$$\frac{d\phi}{dt} = 1 + x^{\gamma+1} \sin\phi' + C_2 G(y) \frac{U'}{L_0^2 x^2}, \tag{C-2}$$

and

$$\frac{dy}{dt} = -\frac{1}{4} \cdot \frac{y}{x} \cdot \frac{I(y)}{f(y)} \cdot \frac{dx}{dt}, \tag{C-3}$$

where dx/dt in 1/[hour:UT], $d\phi/dt$ in [hour:LT] / [hour:UT], $\phi' = C_1\phi$, $U' = \mu/q \cdot y^2$ in [kV/gamma], and $C_1 = -\pi/12$ and $C_2 = -3 \times 10^{12}/a^2\omega \simeq -1016$.

In the case $y = 0$, from equation (16) the third term of equation (C-2) becomes

$$C_3 W_i \frac{x_i^2 \cdot L_0}{x} \tag{C-4}$$

where W_i is an initial energy in keV, x_i an initial position at $t = 0$, and $C_3 = -2 \times 10^3/a^2\omega k_0 \simeq -0.022$.

The above simultaneous differential equations are solved numerically with Hamming's modified predictor-corrector method, an initial condition being $(x, \phi, y, W; t = 0) = (x_i, \phi_i, y_i, W_i)$. Using approximate formulas for f(y), I(y), and G(y) in equations (17), (20), and (22), the solution $(x, \phi, y; t)$ is obtained with sufficient accuracy of 5×10^{-3}, the time step being automatically changed. This accuracy is determined from the observational data by Explorer 45 (S^3-A) which show that the difference in position (x, ϕ) of the particle enhancement between different pitch angle particles is about 10^{-1} (see Fig. 1). The resolution of calculated particle position, therefore, is required to be about 10^{-2}.

FIGURE CAPTIONS

Figure 1. Proton spectrograms of orbit 281 observed by Explorer 45 (S^3 -A) on Feb. 13, 1972. The plasmapause positions during the outbound and inbound portions of the satellite orbit were identified by the DC electric field experiment [Maynard and Cauffman, 1973; Cauffman and Maynard, 1974] at L = 5.1 and L = 4.8, respectively. The satellite position was about L = 5 at 19:20 UT outbound and at 21:35 UT inbound. The magnetic local time at apogee was 19:10 MLT. The typical nose structure in each pitch angle spectrogram is seen inside the plasmapause.

Figure 2a. Change in equatorial pitch angle with L-value. The equatorial pitch angles indicated on the right side are values at L = 10.

Figure 2b. Variations of equatorial pitch angles at various distances indicated by L-values as parameters. The particle which changes its pitch angle beyond the loss cone limit falls into the loss cone.

Figure 3. Changes in particle energy due to radial drift motion. Indicated parameters are initial pitch angles at L = 10. A pitch angle also changes with L as seen in Figure 2, except at 90° and 0°.

Figure 4a - c. The functional values of $f(\alpha_0)$, $I(\alpha_0)$ and $G(\alpha_0)$ as a function of equatorial pitch angle or colatitude of mirror point: $f(0°) = 0.1380172998$, $I(0°) = 0.2760345996$, $G(0°) = 2/3$, $f(90°) = 0.7404804896$, $I(90°) = 0$, and $G(90°) = 1$.

Figure 5a. Relative accuracies of the functions f(y) (dashed line) and I(y) (solid line), with mirror colatitude θ_m, computed from equations (17) and (20). The results from Schulz's approximations are also shown.

Figure 5b. Relative accuracy of the function G(y), with mirror colatitude θ_m, computed from equation (22). The result from Schulz's approximation is also shown.

Figure 6. Kp-dependence of plasmapause position in the case of time-independent electric field model with $\gamma = 2$. L_{STAG} is the distance of the stagnation point at dusk in equation (33), and

Figure 6. (continued) $L_{MIDNIGHT}$ is the distance of crossing point of the last closed equipotential line at the midnight meridian from equation (54). R_b represents the radial distance of McIlwain's injection boundary at each local time; $R_b = (122 - 10\,Kp) / (\phi - 7.3)$ where R_b is L-value and ϕ the local time in hours.

Figure 7. Example of particle trajectories (solid line) in the case $\mu' = 0.083$. Dashed lines represent the stagnation lines through which a particle changes its drift direction. The horizontal open arrows indicate directions of azimuth drift and the vertical open arrows indicate directions of radial drift.

Figure 8. Last closed equipotential lines of zero energy particle with $\gamma = 1$ and 2. The dashed line from dusk to midnight shows McIlwain's injection boundary normalized by the stagnation distance at dusk. The dash-dotted lines are stagnation lines.

Figure 9. The relation of normalized magnetic moment μ' and μ[eV/gamma] with various stagnation distance L_0 as parameters. Two characteristic normalized magnetic moment $\mu'_0 \simeq 0.109$ and $\mu'_{00} \simeq 0.064$ are indicated by dashed lines. The particle having a magnetic moment between these lines (indicated by the dark solid line) takes a flow pattern depicted in Figure 7 or Figure 10e. The upper part shows the particle energy as a function of radial distance L, corresponding to the magnetic moment indicated in the abscissa.

Figure 10a - g. Particle flow patterns (a) electrons, $\mu' = -0.2 < 0$, (b) zero energy particle, $\mu' = 0$, (c) $0 < \mu' = 0.029 < \mu'_{00}$, (d) $\mu' = \mu'_{00} \simeq 0.064$, (e) $\mu'_{00} < \mu' = 0.083 < \mu'_0$, (f) $\mu' = \mu'_0 \simeq 0.109$, and (g) $\mu'_0 < \mu' = 0.2$.

Figure 11a - l. The 90° pitch angle particle tracing computed from equations (C-1) to (C-4). Initial particle positions are at L = 10 and 20:00 MLT $\leq \phi <$ 4:00 MLT at 0.1 hour interval. Particle positions are represented by dots at 0.1 hour (= 6 min) steps and by asterisks at 1 hour steps within 20 hours and L $\leq$ 10. Stagnation distance is $L_0 = 5$, constant. The initial particle energies W_i at L = 10 are; (a) -0.4 keV (electron), (b) 0, (c) 0.1 keV, (d) 0.2 keV, (e) 0.4 keV, (f) 0.8 keV, (g) 1.6 keV, (h) 3.2 keV, (i) 6.4 keV, (j) 12.8 keV, (k) 25.6 keV, and (l) 51.2 keV.

Figure 12a - d. The trajectories of particles with the energy of 0.566 keV at L = 10, and pitch angles of (a) 0°, (b) 30°, (c) 60°, and (d) 90°. See the caption of Figure 11.

Figure 13. The difference of particle flow fronts due to pitch angles, 0° and 90°. Initial particle positions and electric field intensity are the same as Figure 12. Particle energies at L = 10 are 1.6 keV for 0° particles and 0.8 keV for 90° particles, and these particle energies are approximately equal at L = 3.5.

Figure 1.

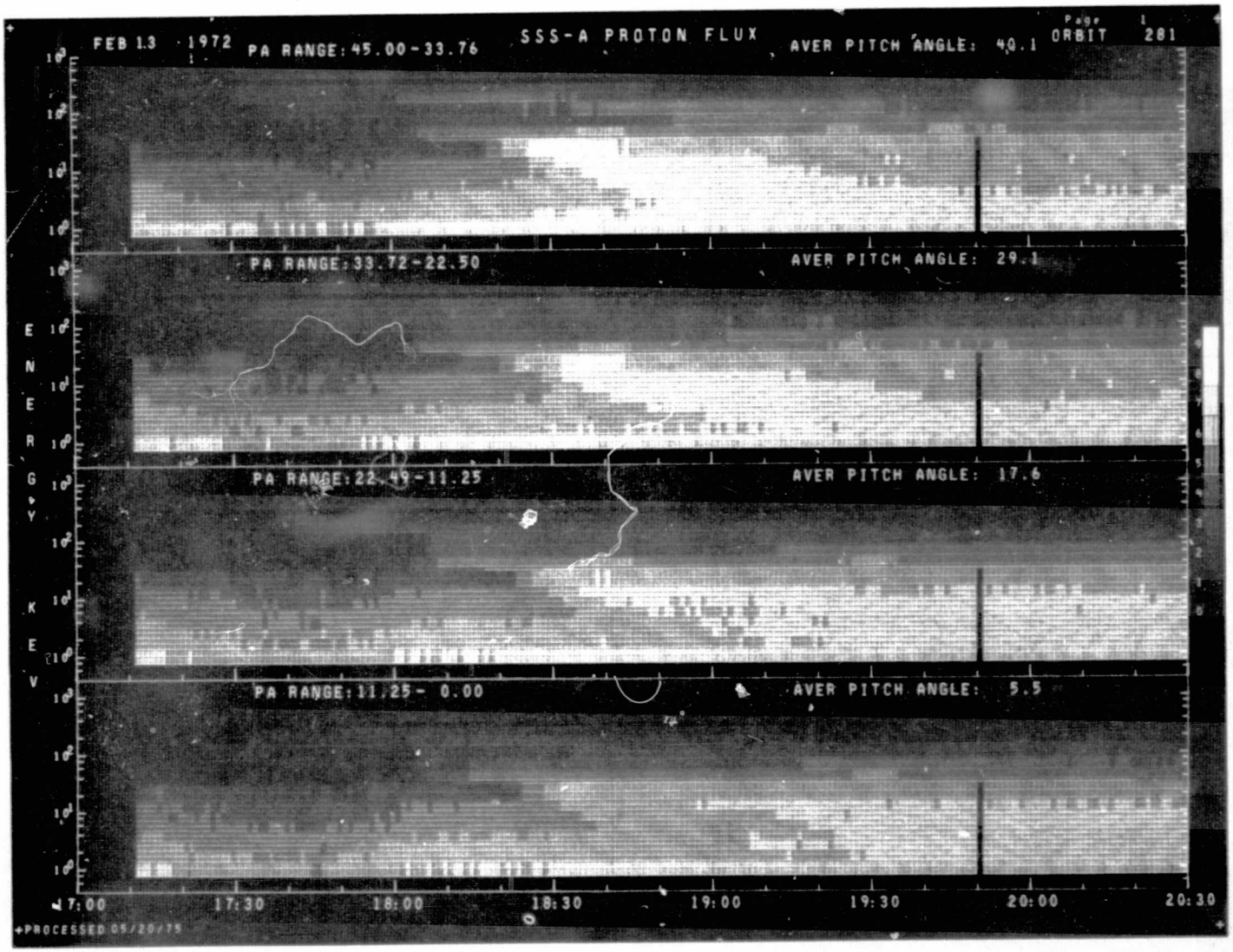

Figure 1 (Continued).

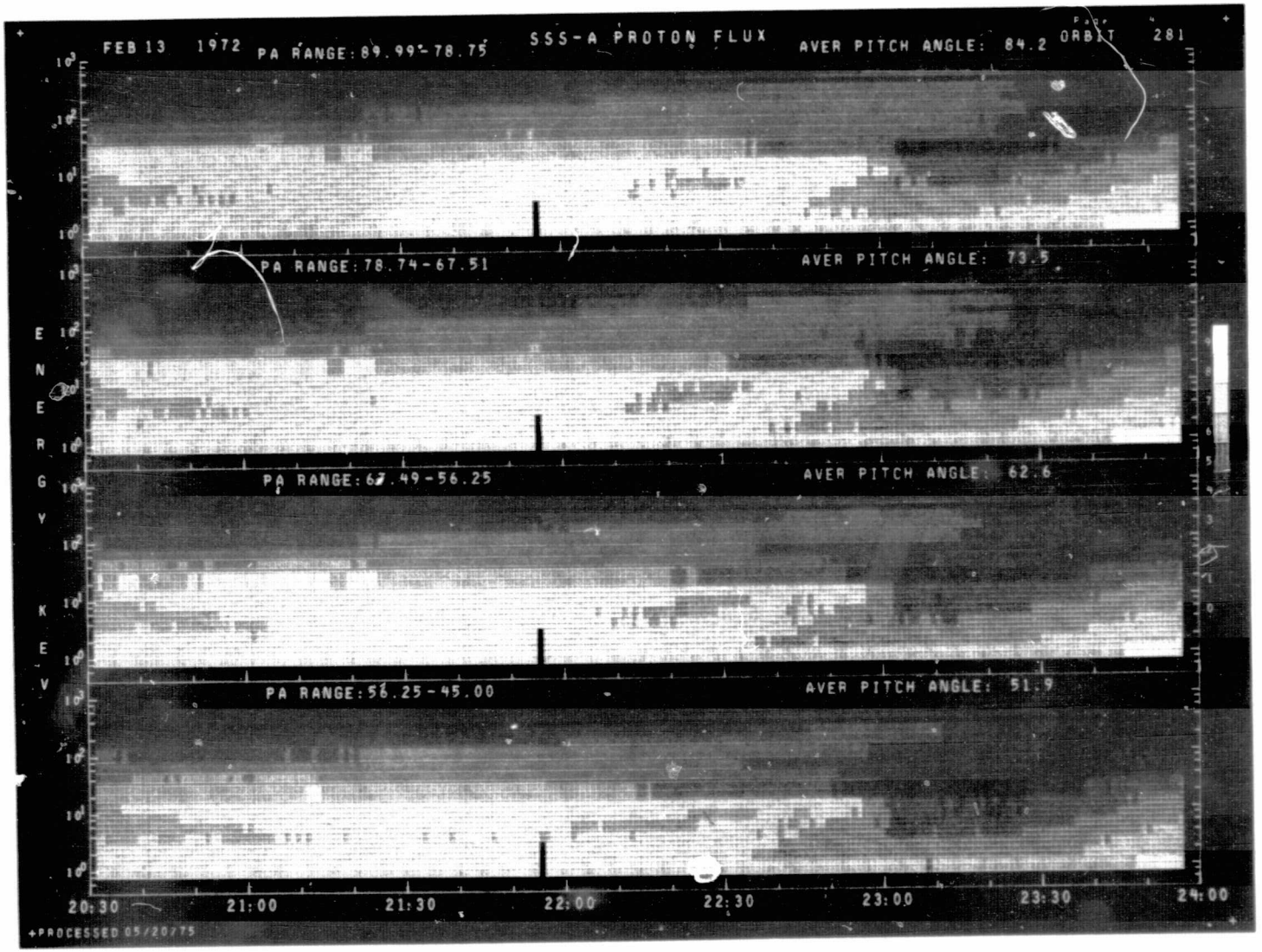

Figure 1 (Continued)

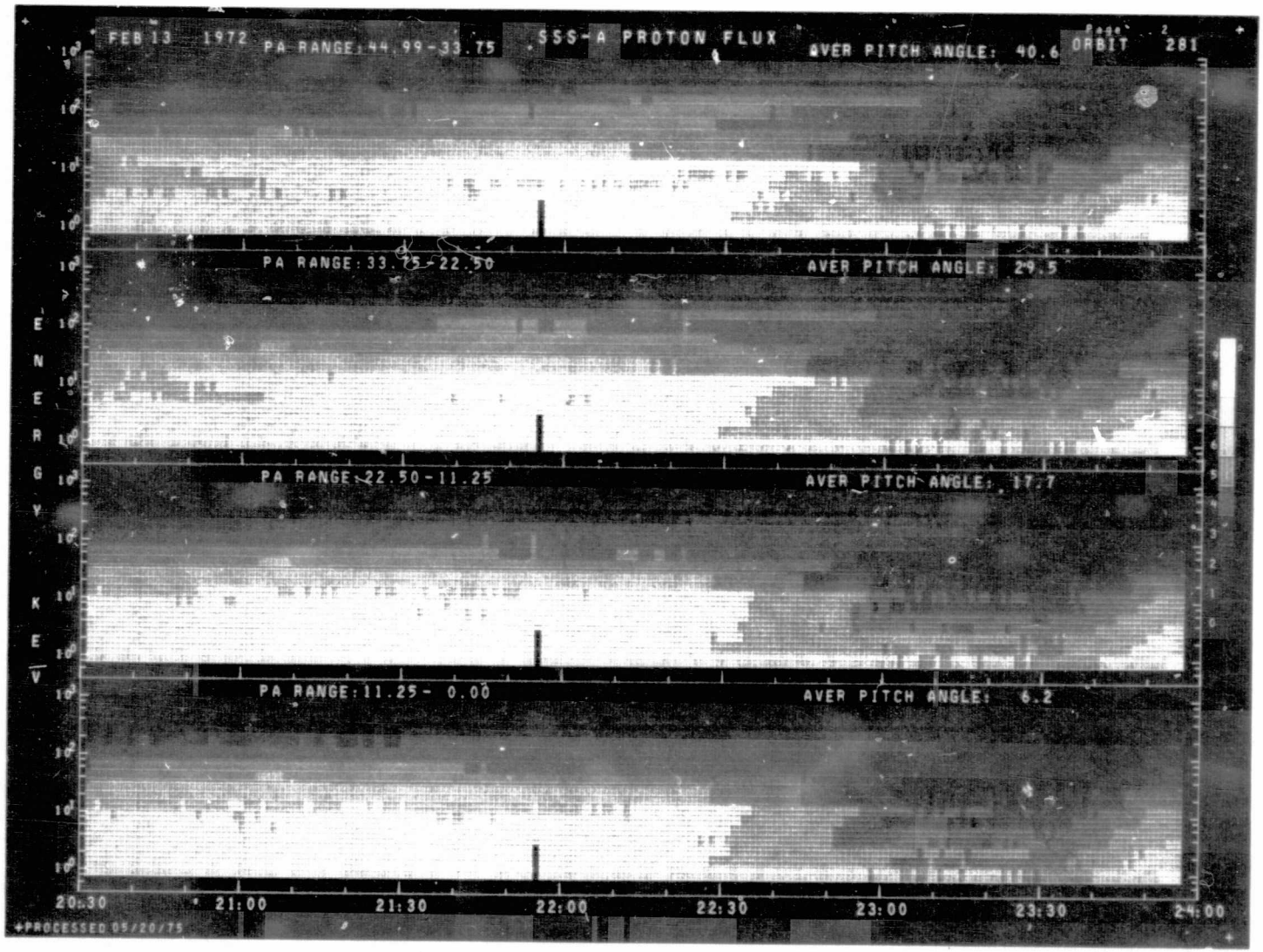

Figure 1 (Continued)

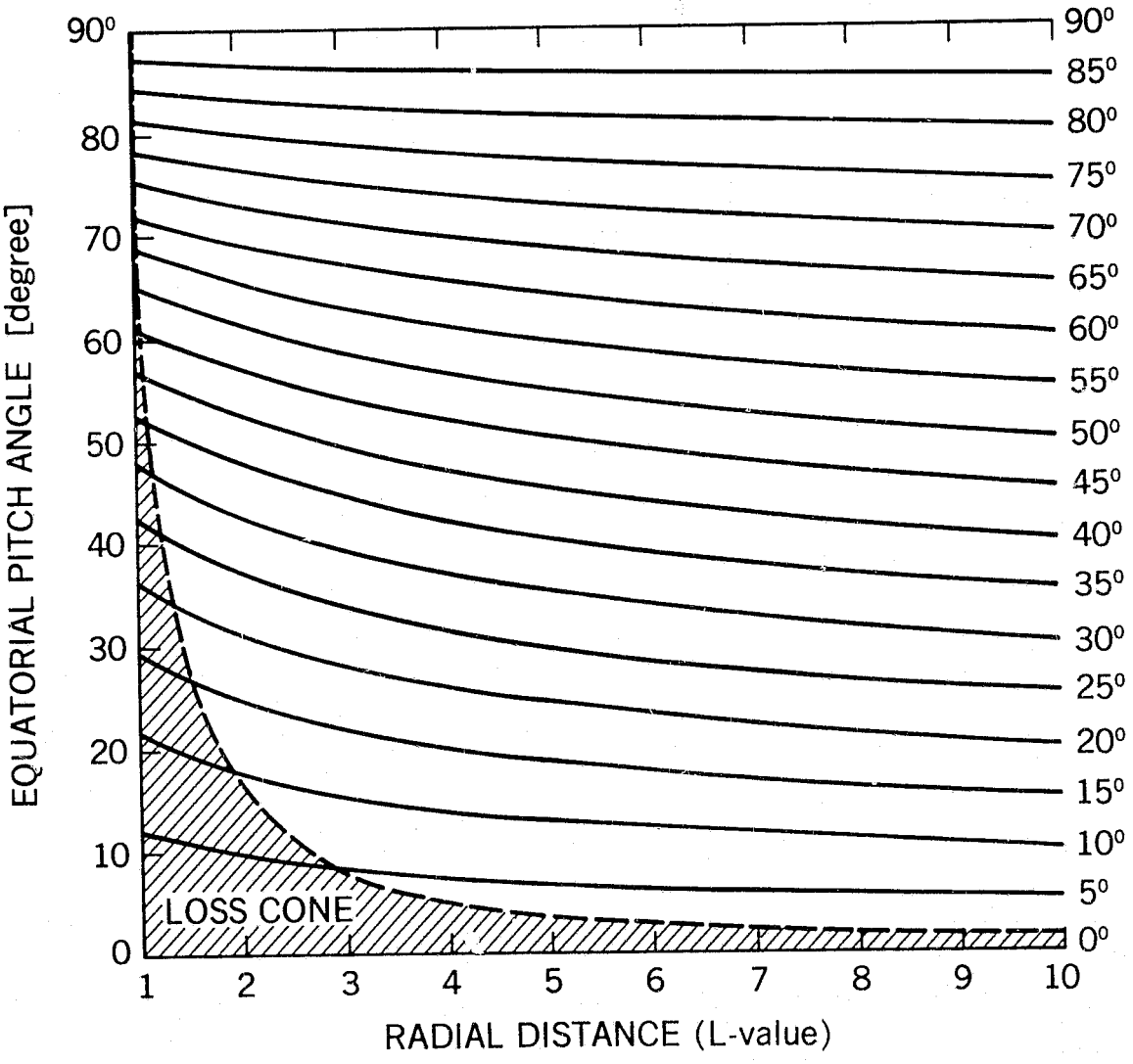
EQUATORIAL PITCH ANGLE [degree]
90°
80
70
60
50
40
30
20
10
0
LOSS CONE
1
2
3
4
5
6
7
8
9
10
RADIAL DISTANCE (L-value)
90°
85°
80°
75°
70°
65°
60°
55°
50°
45°
40°
35°
30°
25°
20°
15°
10°
5°
0°

Figure 2a.

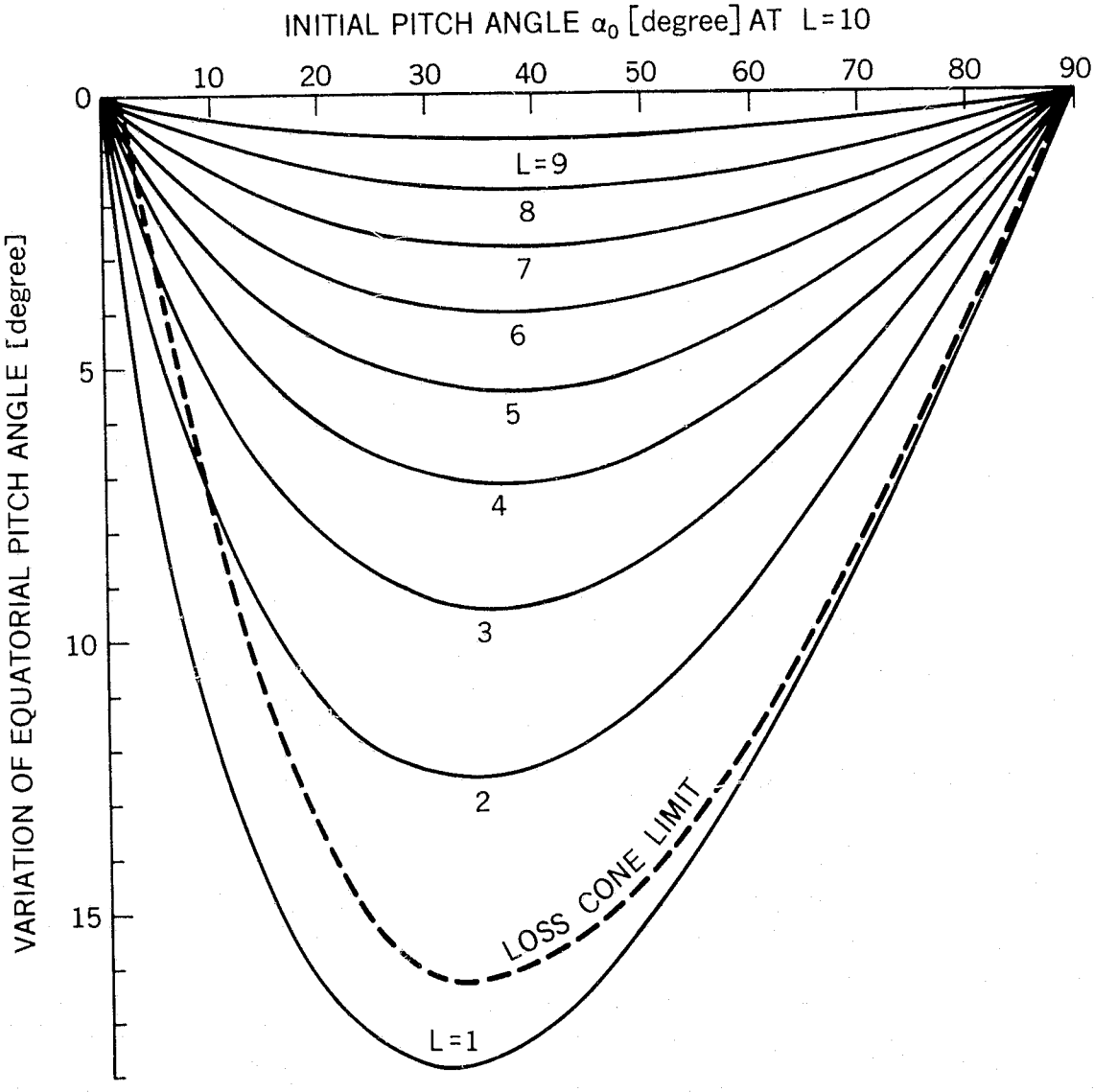
INITIAL PITCH ANGLE α_0 [degree] AT L=10
10
20
30
40
50
60
70
80
90
0
5
10
15
VARIATION OF EQUATORIAL PITCH ANGLE [degree]
L=9
8
7
6
5
4
3
2
LOSS CONE LIMIT
L=1

Figure 2b.

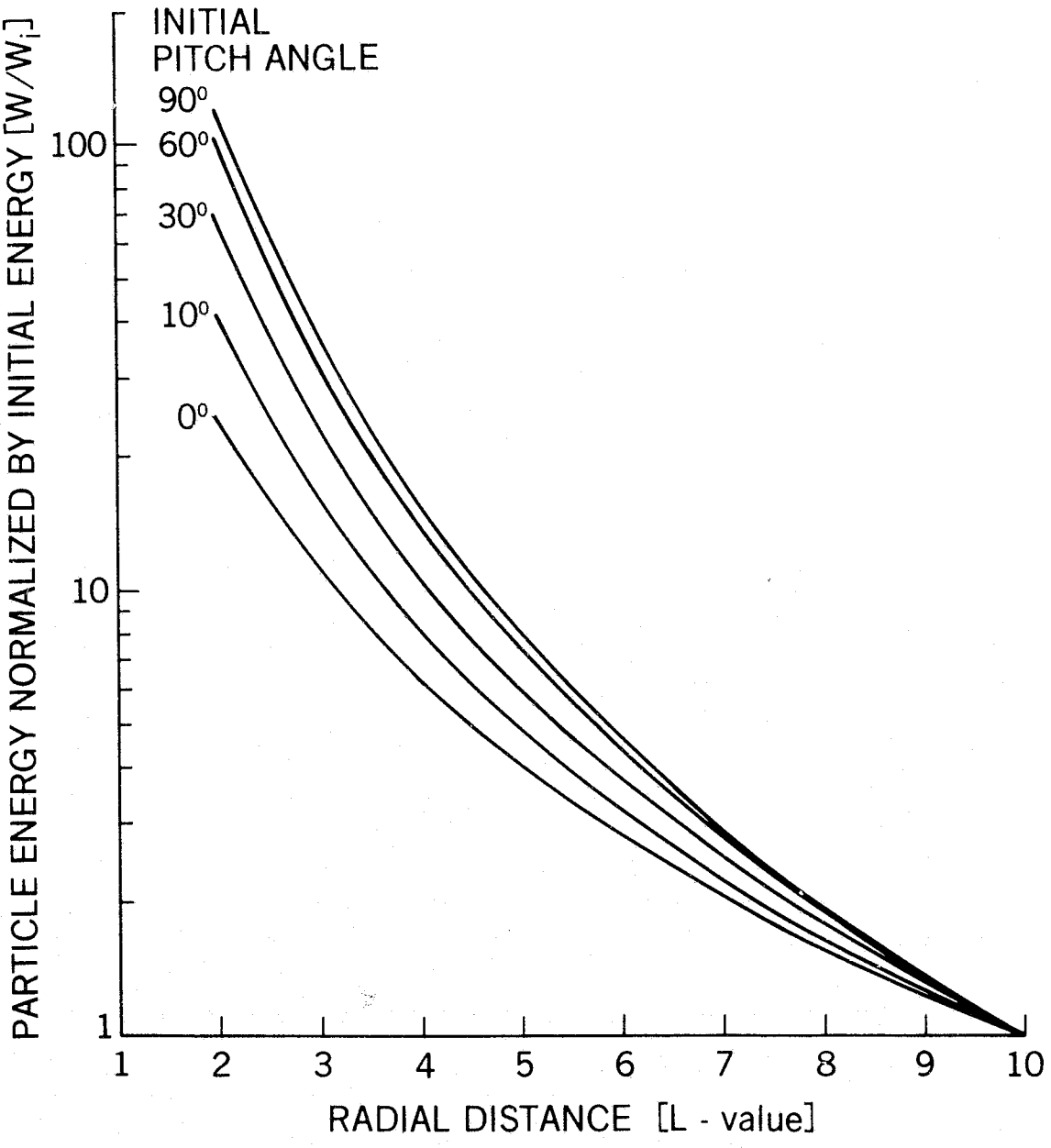
INITIAL
PITCH ANGLE
90°
60°
30°
10°
0°
100
10
1
PARTICLE ENERGY NORMALIZED BY INITIAL ENERGY [W/W_i]
1
2
3
4
5
6
7
8
9
10
RADIAL DISTANCE [L - value]

Figure 3.

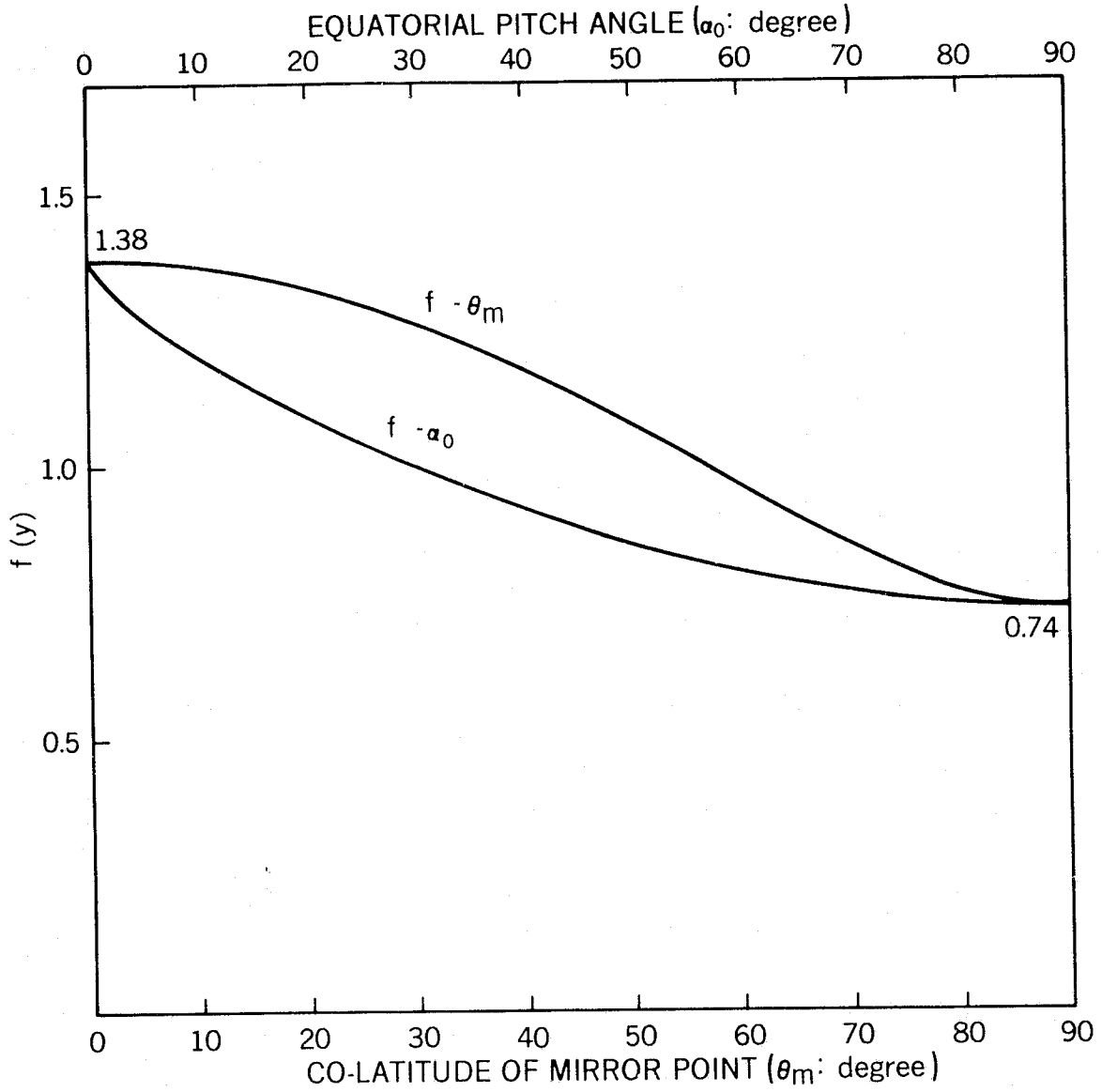
EQUATORIAL PITCH ANGLE (α_0: degree)
0
10
20
30
40
50
60
70
80
90
1.5
1.38
f - θ_m
f - α_0
1.0
f (y)
0.74
0.5
0
10
20
30
40
50
60
70
80
90
CO-LATITUDE OF MIRROR POINT (θ_m: degree)

Figure 4a.

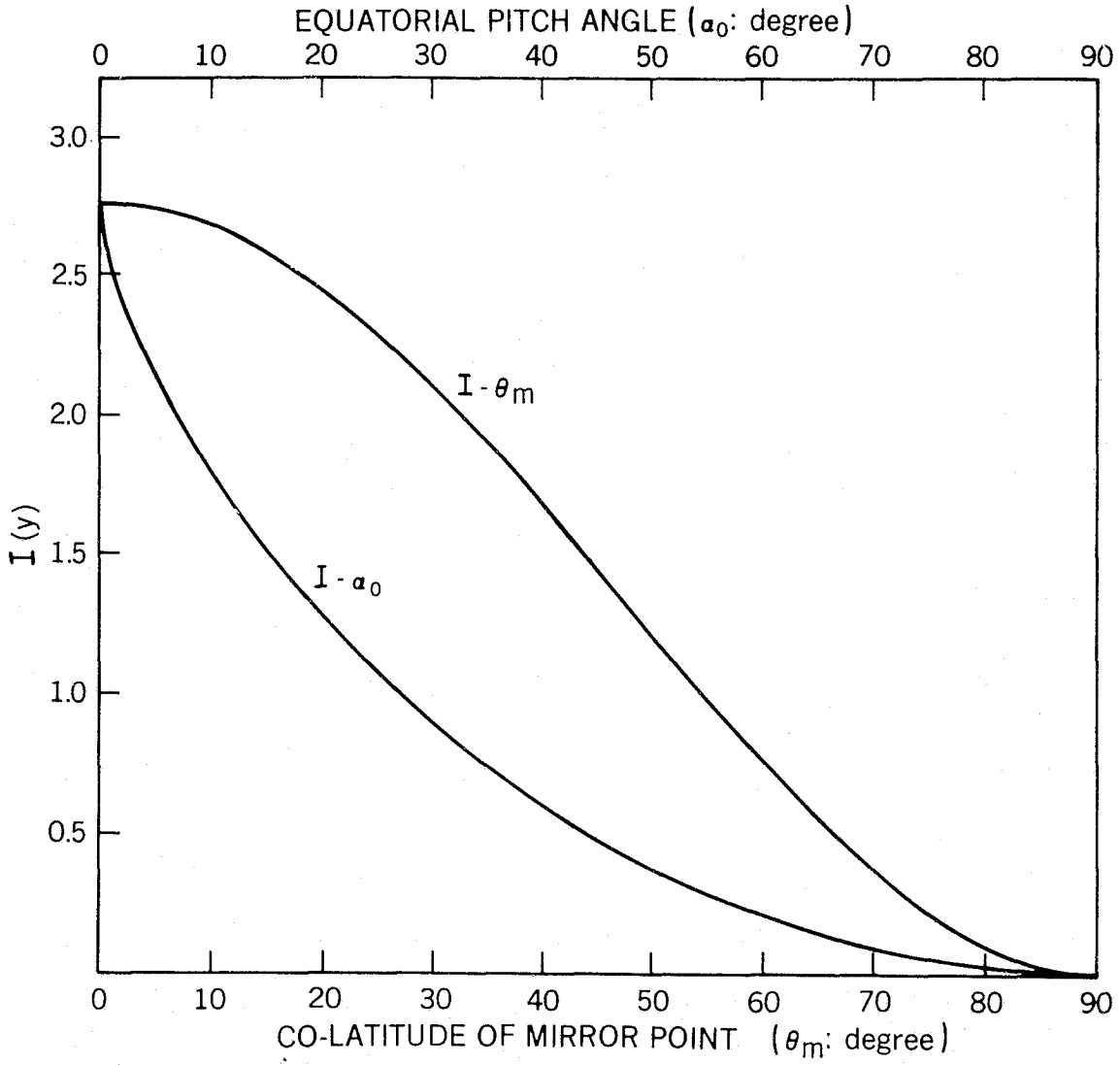
EQUATORIAL PITCH ANGLE (α_0: degree)
0
10
20
30
40
50
60
70
80
90
3.0
2.5
2.0
1.5
1.0
0.5
I (y)
I - θ_m
I - α_0
CO-LATITUDE OF MIRROR POINT (θ_m: degree)

Figure 4b.

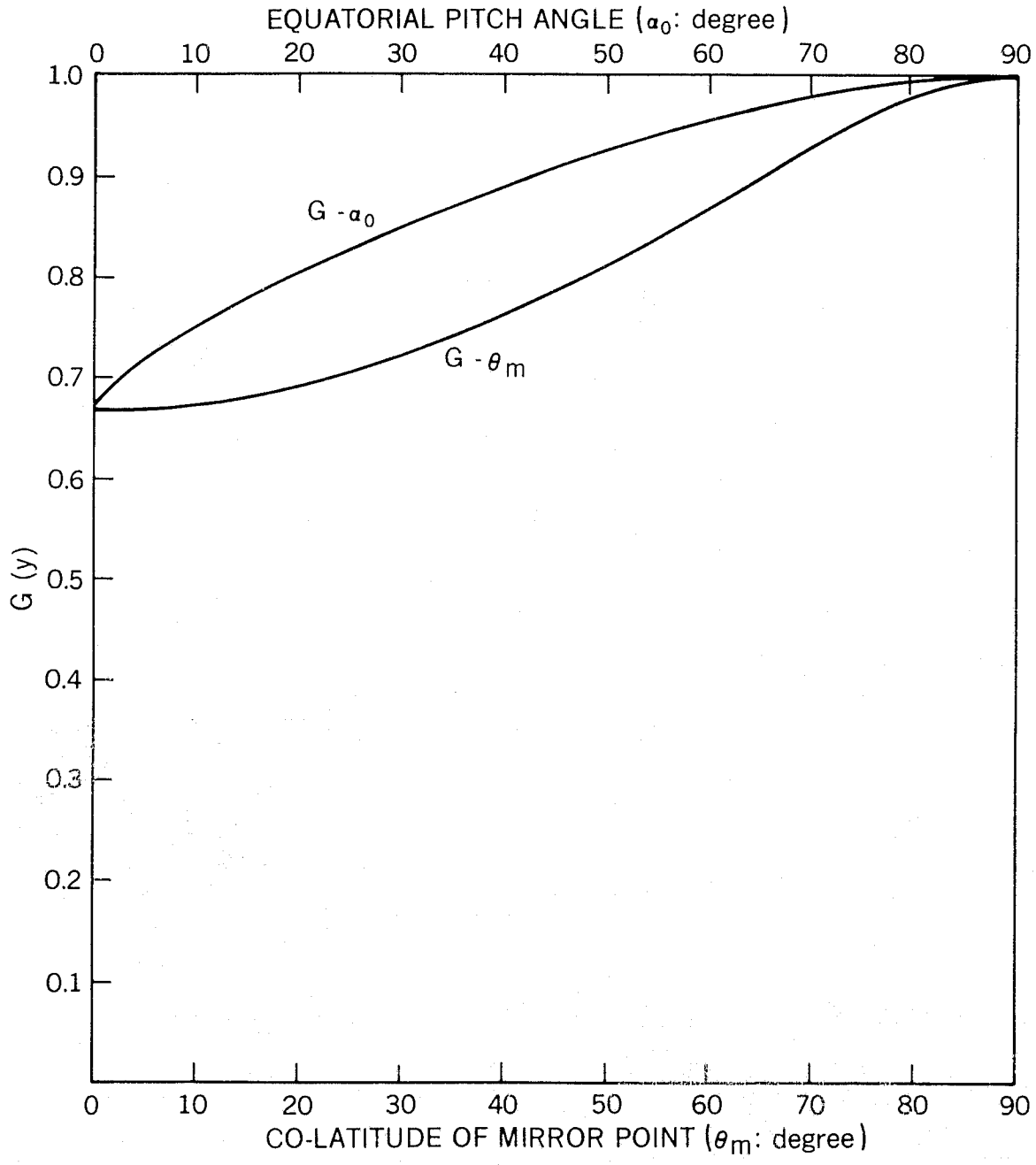
EQUATORIAL PITCH ANGLE (α_0: degree)
0
10
20
30
40
50
60
70
80
90
1.0
0.9
0.8
0.7
0.6
0.5
0.4
0.3
0.2
0.1
G (y)
G - α_0
G - θ_m
CO-LATITUDE OF MIRROR POINT (θ_m: degree)

Figure 4c.

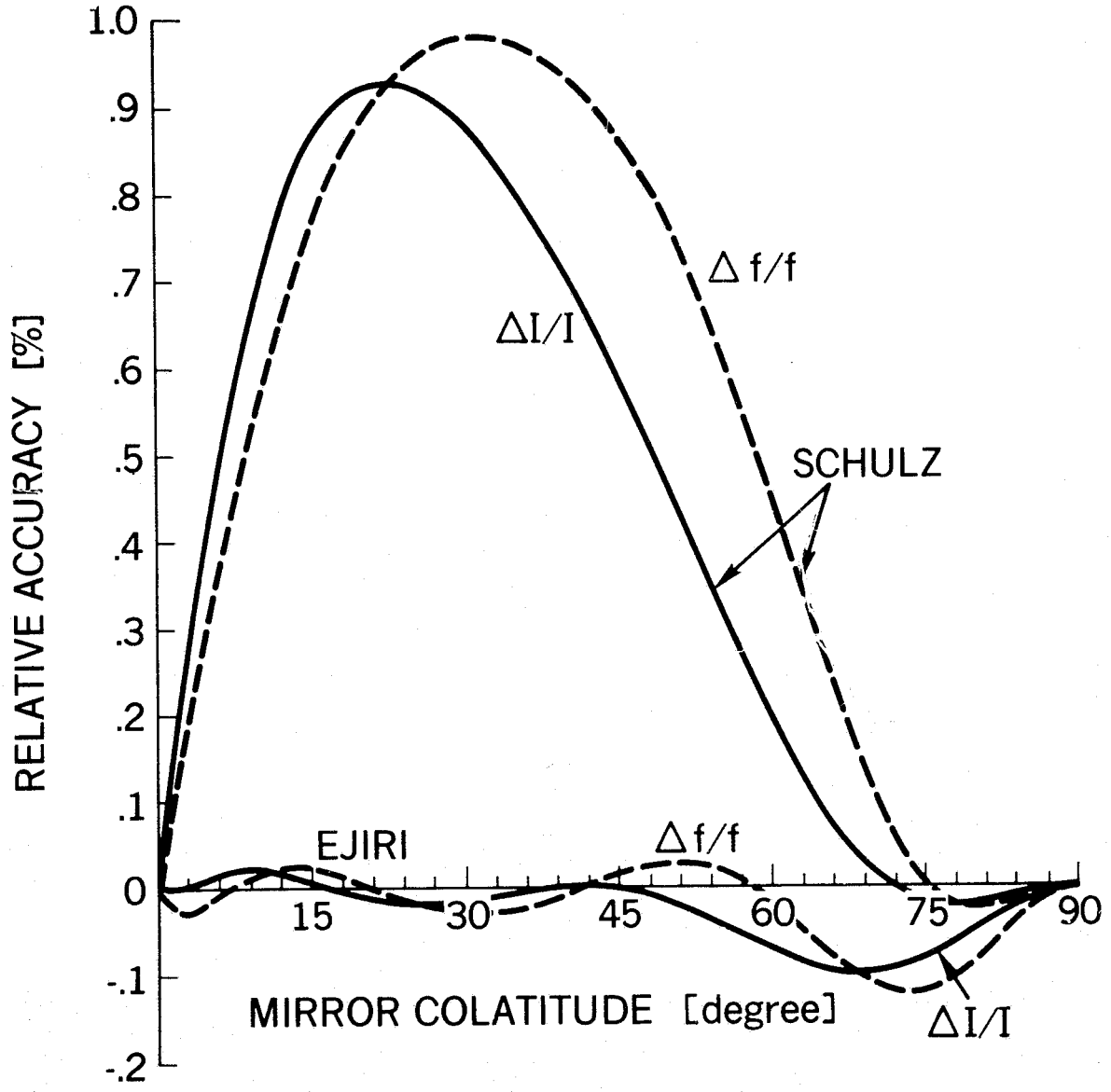
1.0
.9
.8
.7
.6
.5
.4
.3
.2
.1
0
-.1
-.2
RELATIVE ACCURACY [%]
Δ f/f
ΔI/I
SCHULZ
EJIRI
Δ f/f
15
30
45
60
75
90
MIRROR COLATITUDE [degree]
ΔI/I

Figure 5a.

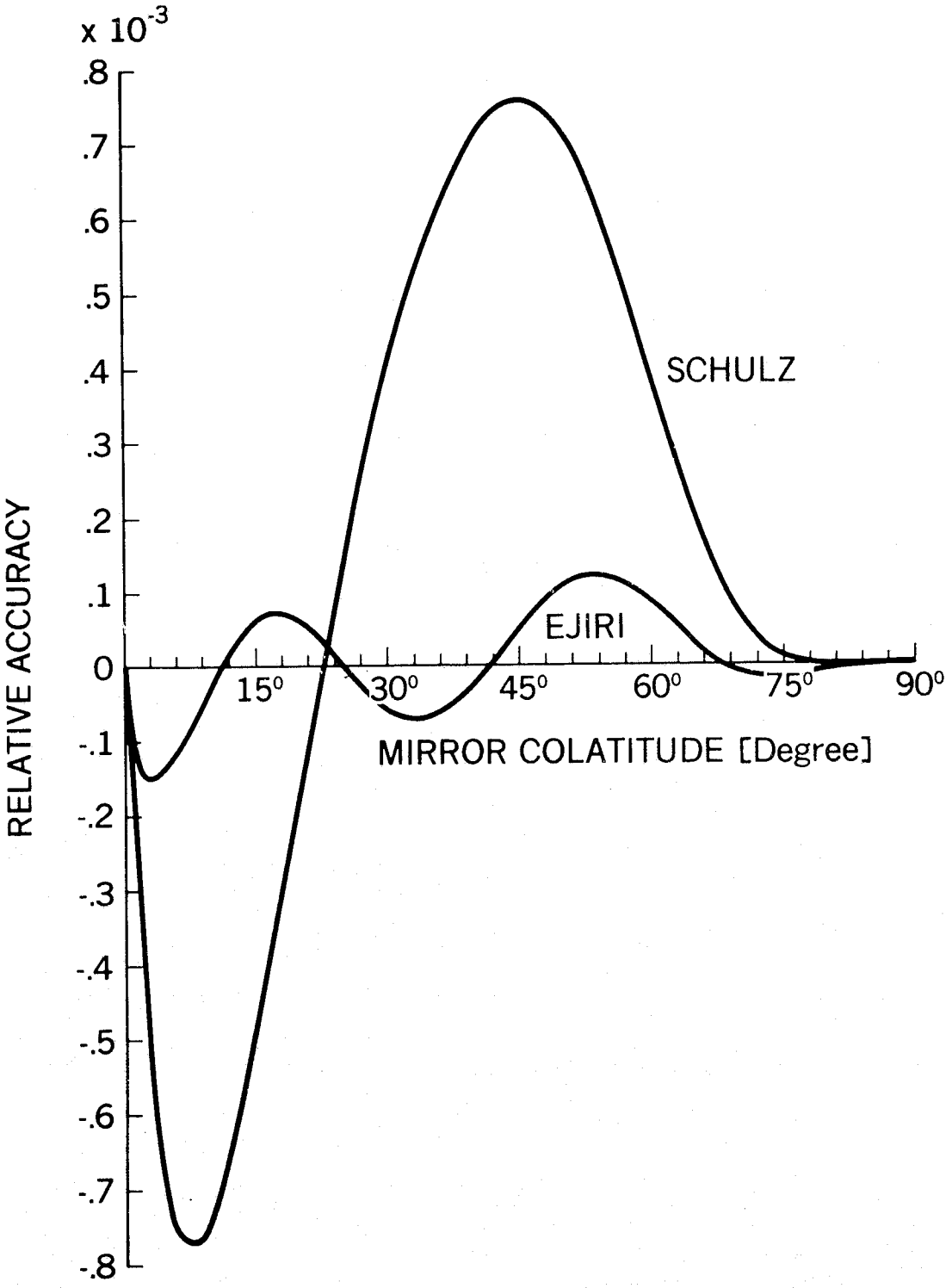
x 10-3
.8
.7
.6
.5
.4
.3
.2
.1
0
-.1
-.2
-.3
-.4
-.5
-.6
-.7
-.8
RELATIVE ACCURACY
SCHULZ
EJIRI
15°
30°
45°
60°
75°
90°
MIRROR COLATITUDE [Degree]

Figure 5b.

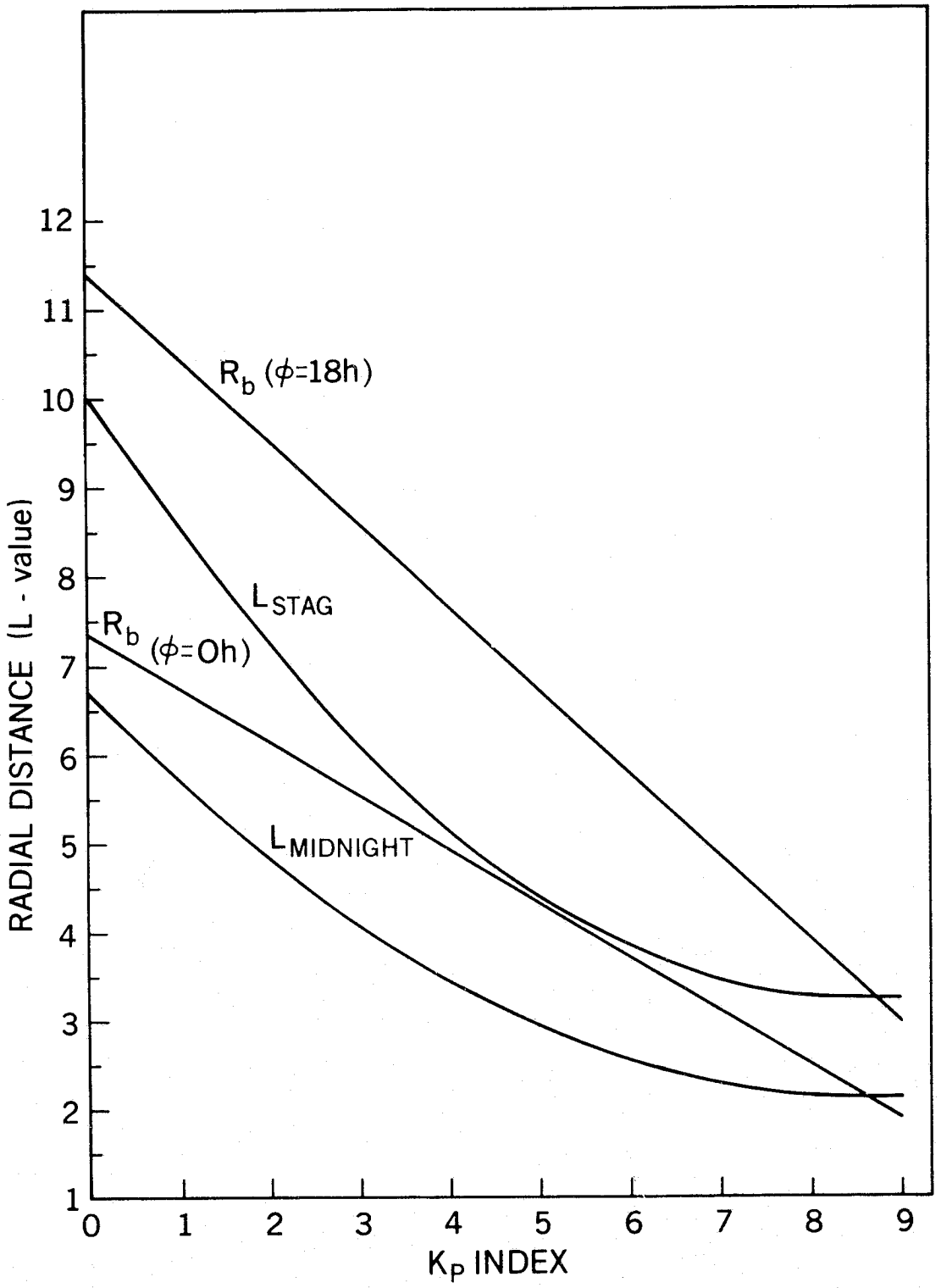
RADIAL DISTANCE (L - value)
12
11
10
9
8
7
6
5
4
3
2
1
0
1
2
3
4
5
6
7
8
9
K_P INDEX
R_b (ϕ=18h)
L_{STAG}
R_b (ϕ=Oh)
$L_{MIDNIGHT}$

Figure 6.

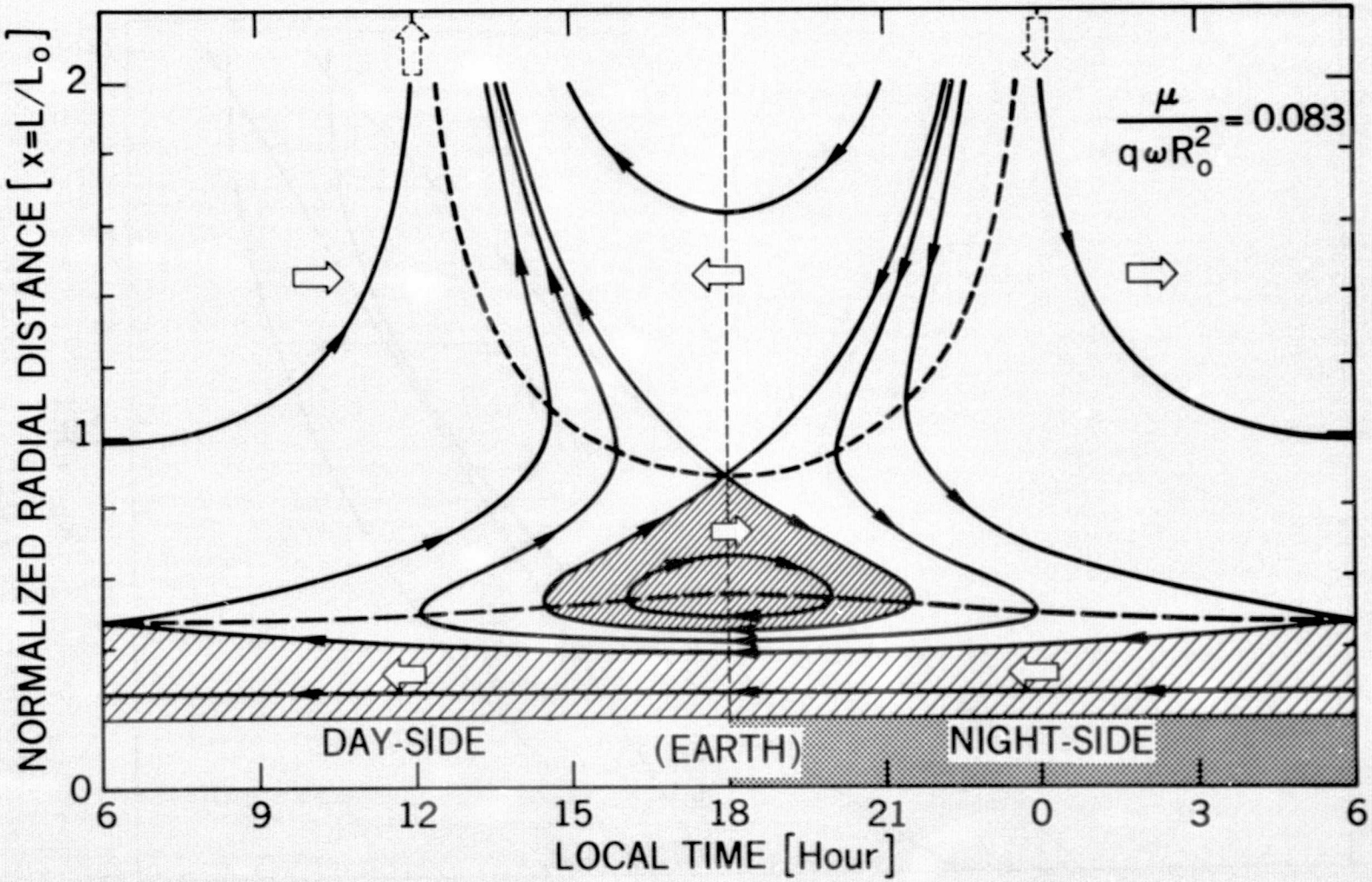
NORMALIZED RADIAL DISTANCE [x=L/L₀]
2
1
0
$\frac{\mu}{q\omega R_o^2} = 0.083$
DAY-SIDE
(EARTH)
NIGHT-SIDE
6
9
12
15
18
21
0
3
6
LOCAL TIME [Hour]

Figure 7.

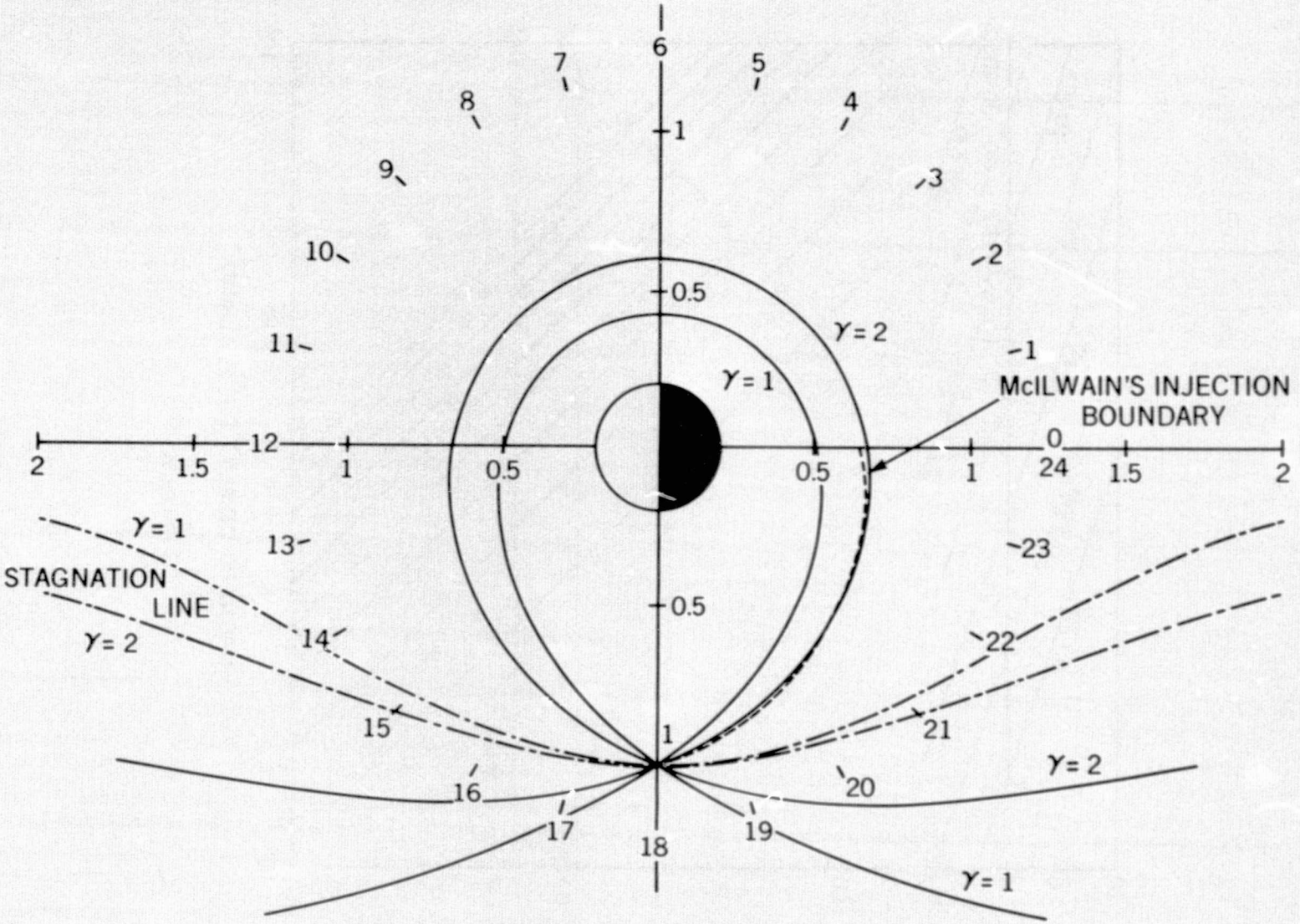
6
7
5
8
4
1
9
3
10
2
0.5
γ = 2
11
-1
γ = 1
McILWAIN'S INJECTION
BOUNDARY
2
1.5
12
1
0.5
0.5
1
0
24
1.5
2
γ = 1
13
23
STAGNATION
LINE
0.5
γ = 2
14
22
15
21
1
γ = 2
16
20
17
19
18
γ = 1

Figure 8.

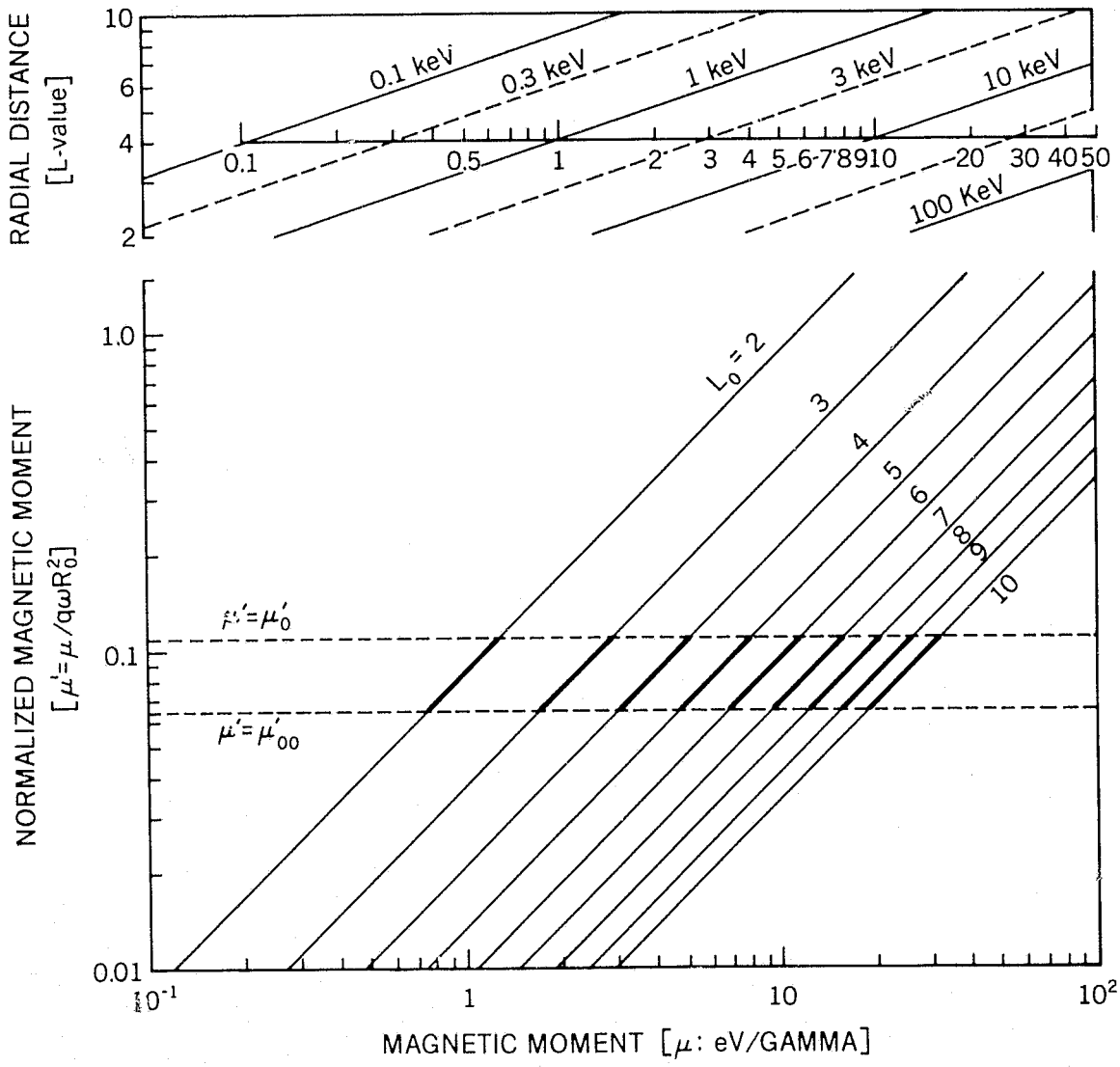
RADIAL DISTANCE
[L-value]
10
6
4
2
0.1 keV
0.3 keV
1 keV
3 keV
10 keV
100 KeV
0.1
0.5
1
2
3
4
5
6
7
8
9
10
20
30
40
50
NORMALIZED MAGNETIC MOMENT
[μ'=μ/qωR0²]
1.0
0.1
0.01
L0 = 2
3
4
5
6
7
8
9
10
μ'=μ'0
μ'=μ'00
10⁻¹
1
10
10²
MAGNETIC MOMENT [μ: eV/GAMMA]

Figure 9.

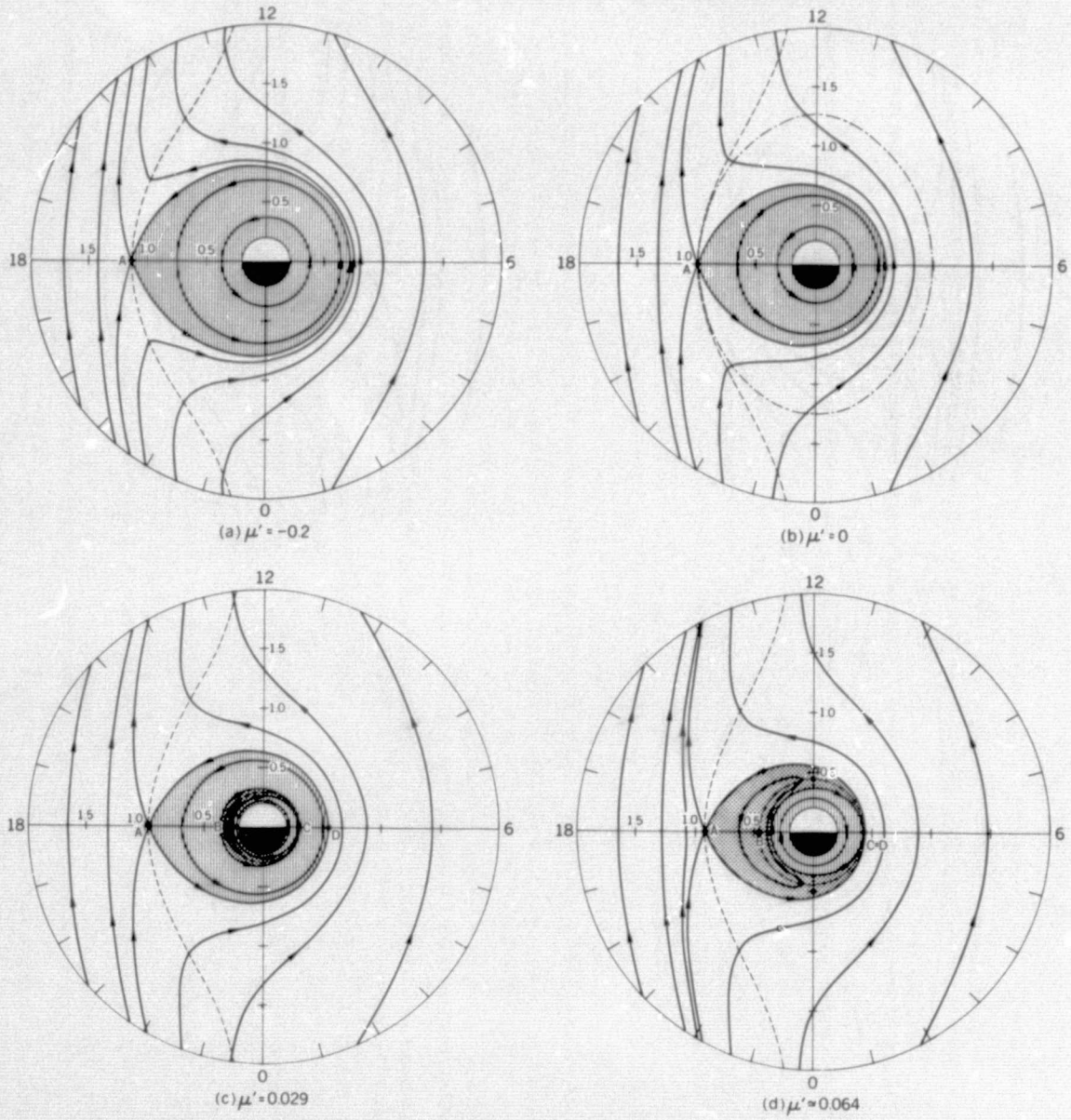

Figure 10.

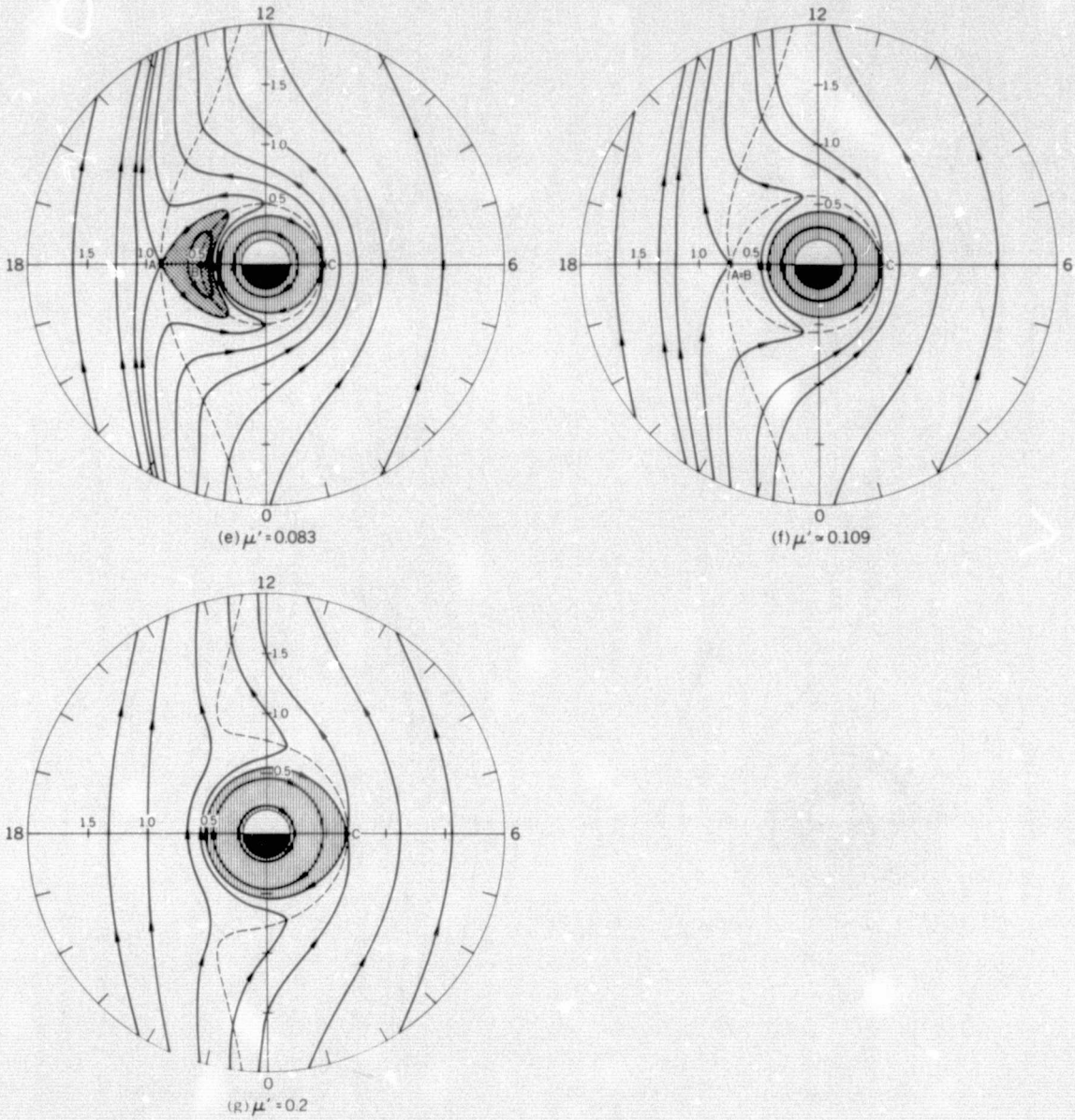

Figure 10 (Continued).

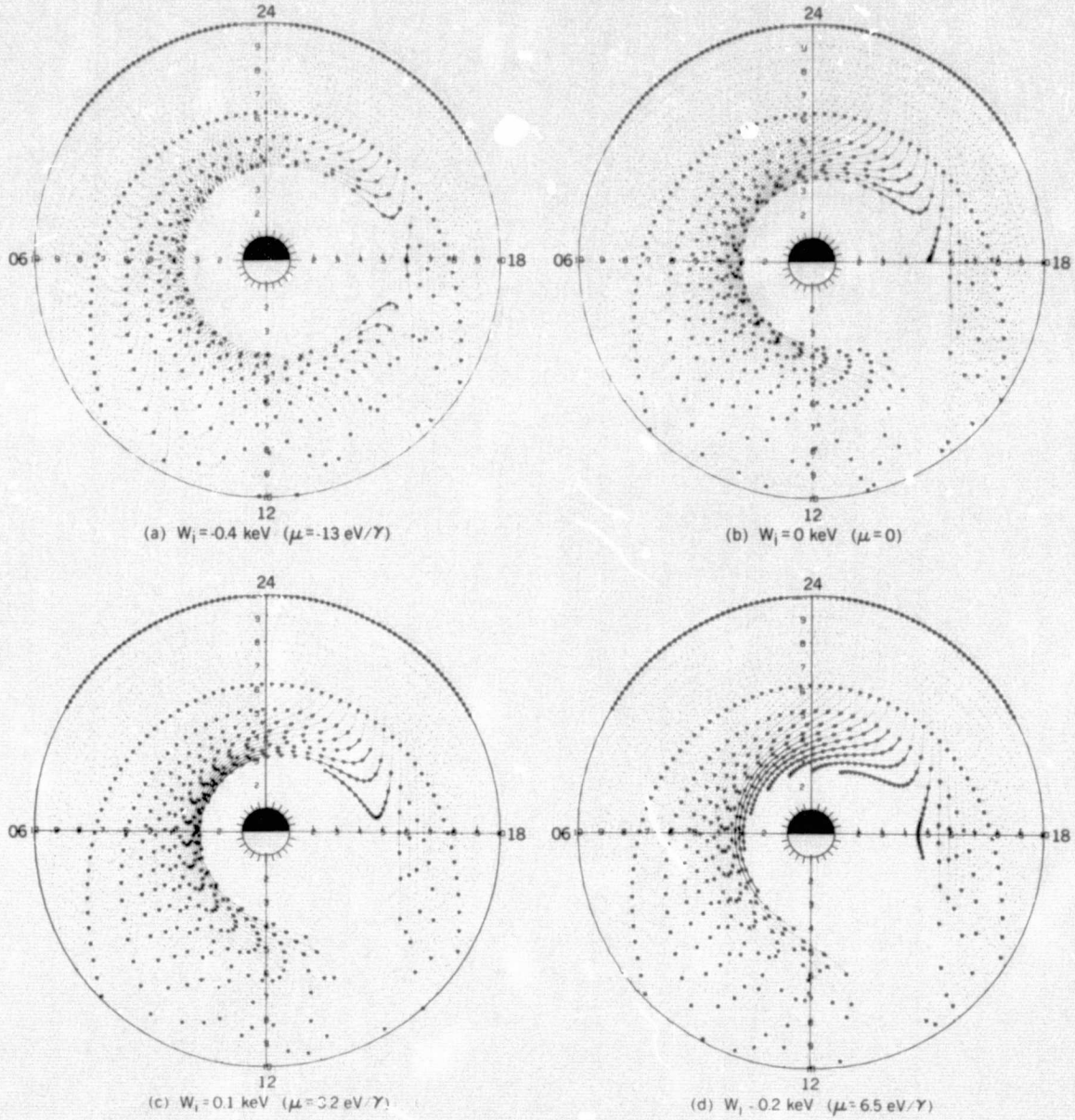

(a) $W_i = -0.4$ keV ($\mu = -13$ eV/γ)

(b) $W_i = 0$ keV ($\mu = 0$)

(c) $W_i = 0.1$ keV ($\mu = 3.2$ eV/γ)

(d) $W_i = 0.2$ keV ($\mu = 6.5$ eV/γ)

Figure 11.

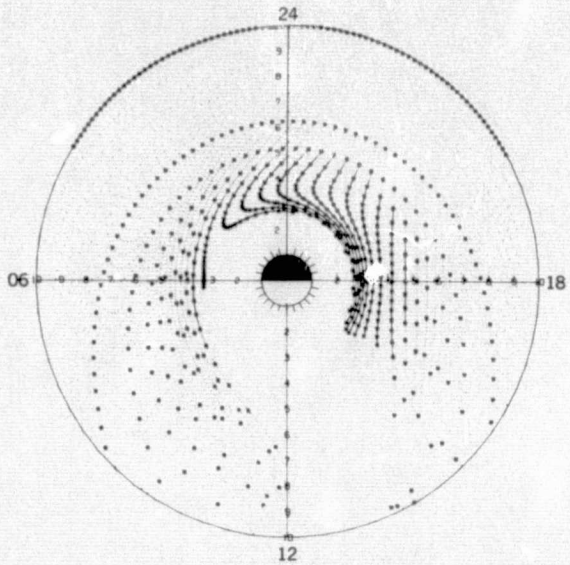

(e) $W_i = 0.4$ keV ($\mu = 13$ eV/γ)

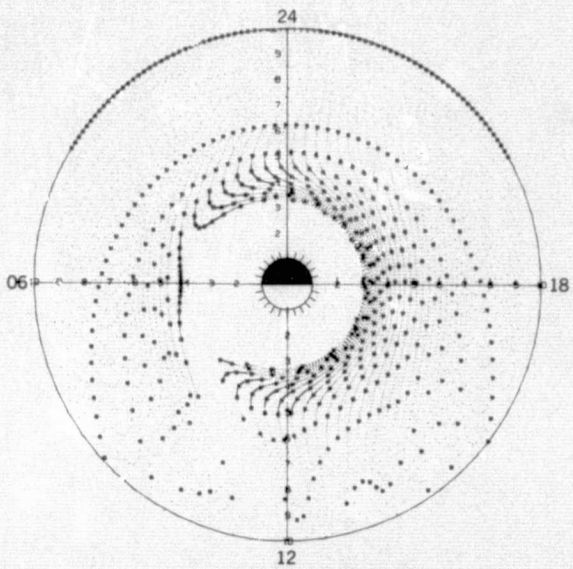

(f) $W_i = 0.8$ keV ($\mu = 26$ eV/γ)

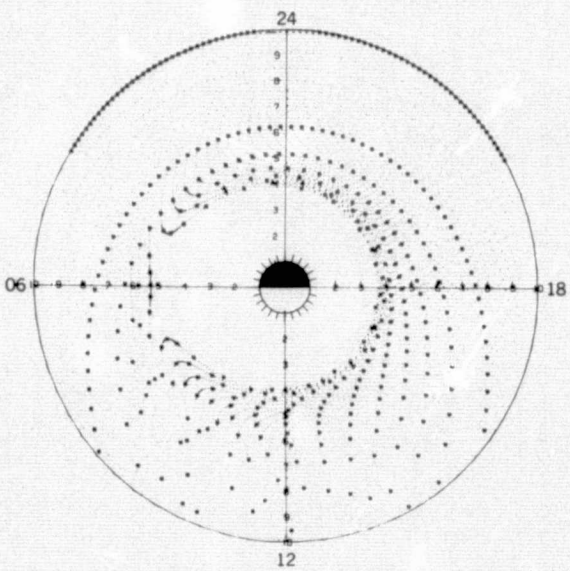

(g) $W_i = 1.6$ keV ($\mu = 52$ eV/γ)

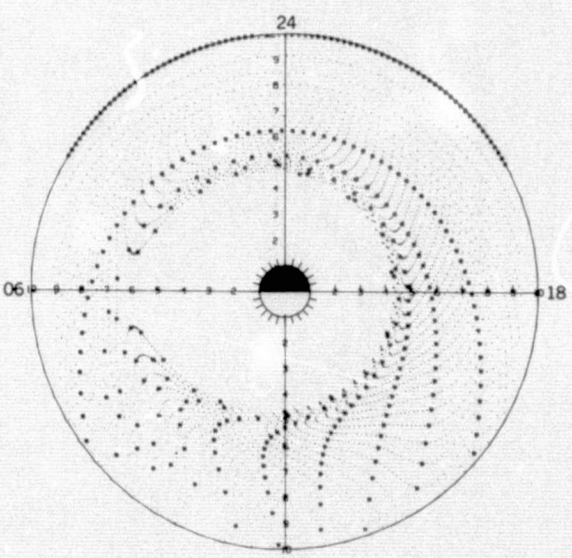

(h) $W_i = 3.2$ keV ($\mu = 103$ eV/γ)

Figure 11 (Continued).

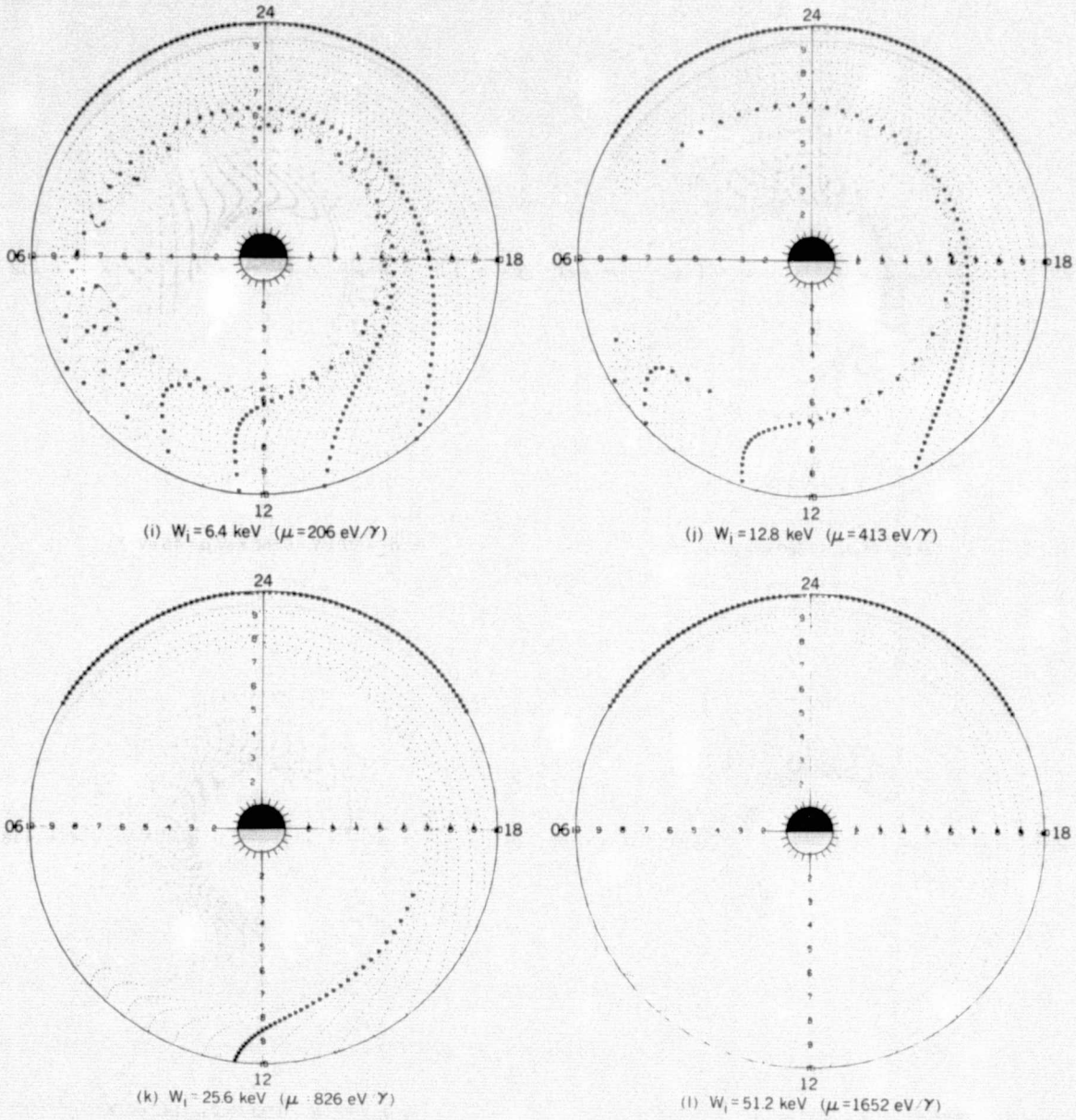

(i) $W_i = 6.4$ keV ($\mu = 206$ eV/γ)

(j) $W_i = 12.8$ keV ($\mu = 413$ eV/γ)

(k) $W_i = 25.6$ keV ($\mu = 826$ eV/γ)

(l) $W_i = 51.2$ keV ($\mu = 1652$ eV/γ)

Figure 11 (Continued).

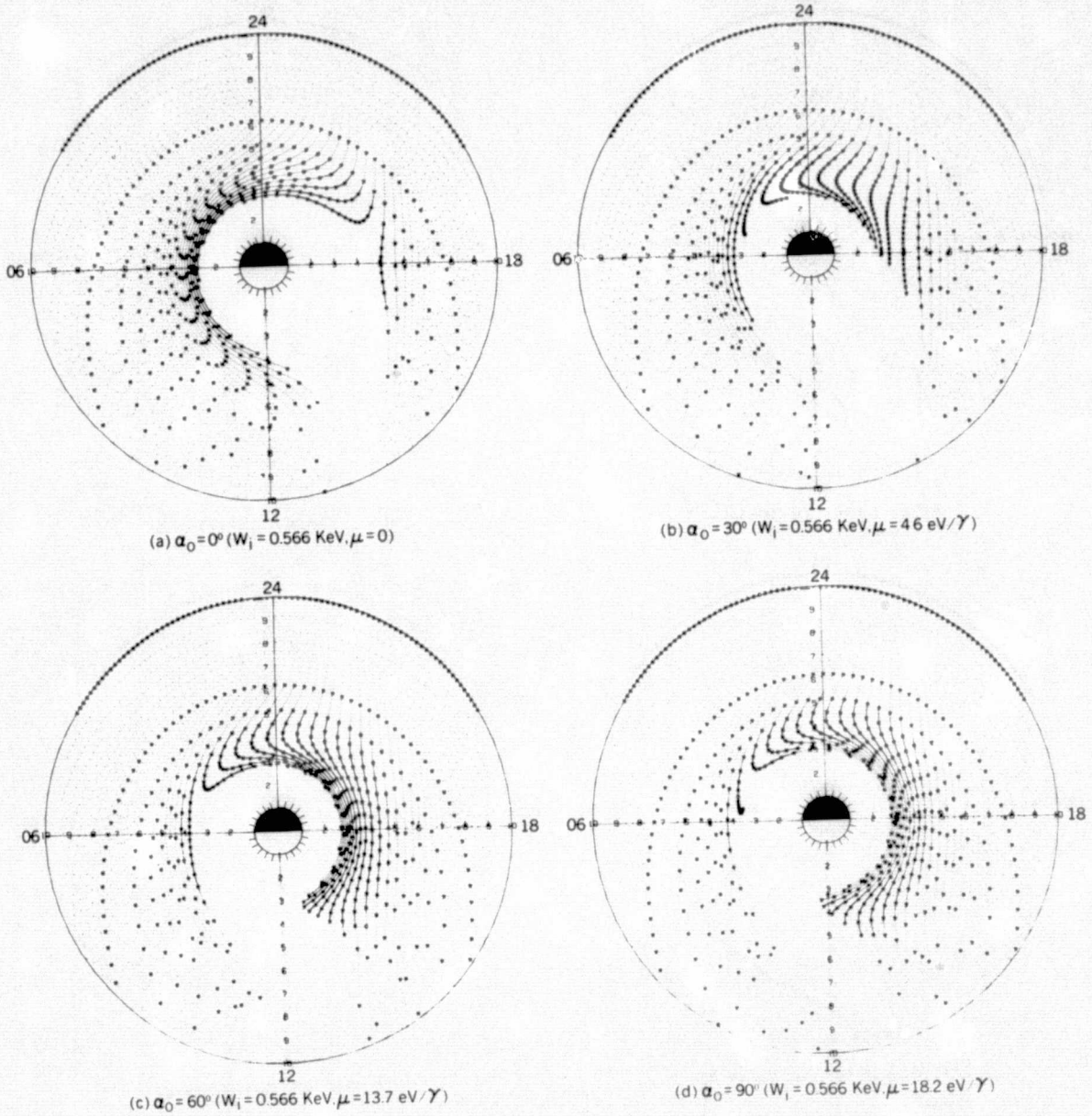
24
06
18
12
(a) $\alpha_0 = 0^\circ$ ($W_i = 0.566$ KeV, $\mu = 0$)
(b) $\alpha_0 = 30^\circ$ ($W_i = 0.566$ KeV, $\mu = 4.6$ eV/γ)
(c) $\alpha_0 = 60^\circ$ ($W_i = 0.566$ KeV, $\mu = 13.7$ eV/γ)
(d) $\alpha_0 = 90^\circ$ ($W_i = 0.566$ KeV, $\mu = 18.2$ eV/γ)

Figure 12.

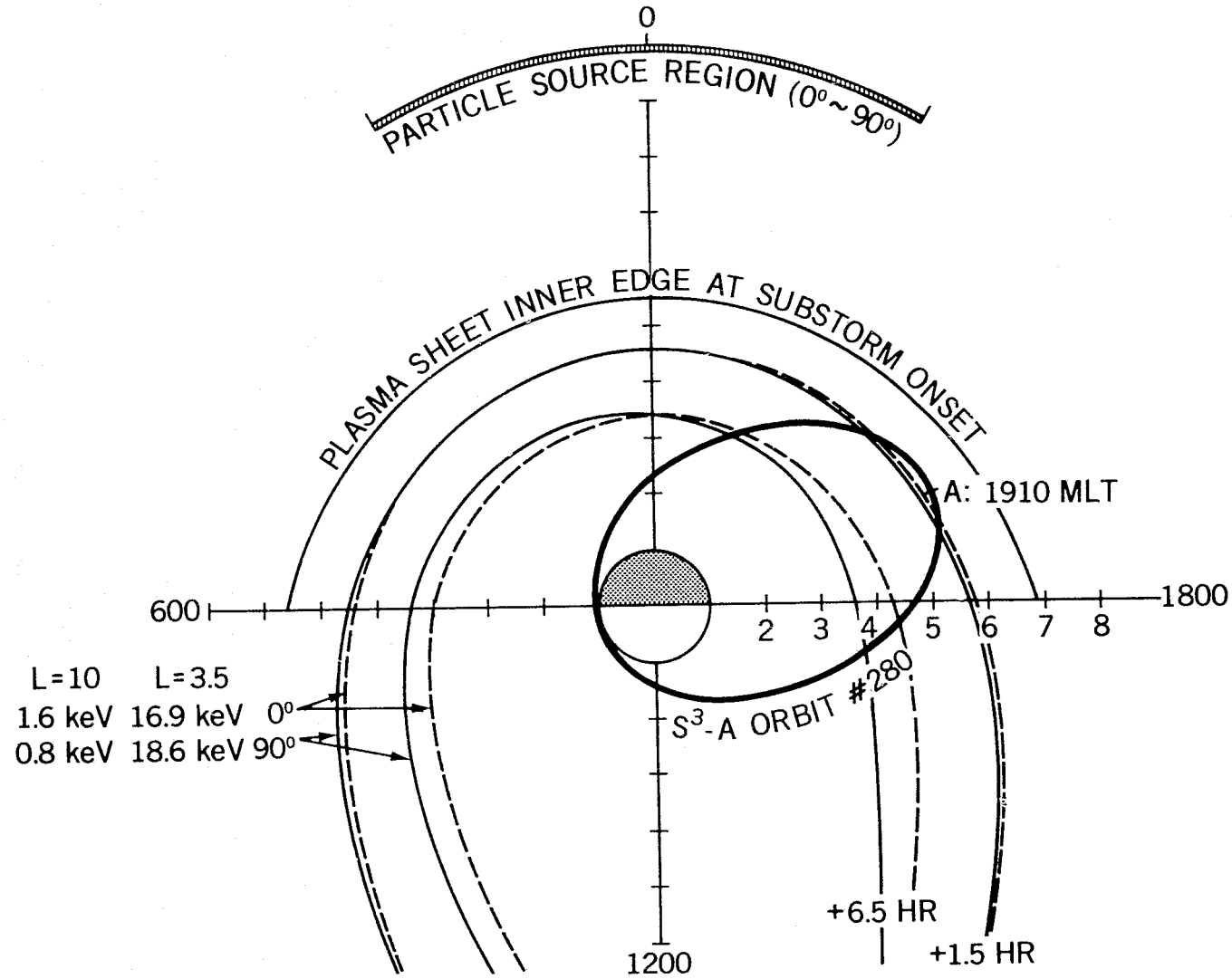
0
PARTICLE SOURCE REGION (0°~90°)
PLASMA SHEET INNER EDGE AT SUBSTORM ONSET
A: 1910 MLT
600
1800
2
3
4
5
6
7
8
L=10
L=3.5
1.6 keV
16.9 keV
0°
0.8 keV
18.6 keV
90°
S3-A ORBIT #280
+6.5 HR
+1.5 HR
1200

Figure 13.